Inhibition of photoferrotrophy by nitric oxide in ferruginous environments

Verena Nikeleit[1], Adrian Mellage[2], Giorgio Bianchini[3], Lea Sauter[1], Steffen Buessecker[4,5], Stefanie Gotterbarm[1], Manuel Schad[1], Kurt Konhauser[6], Aubrey L. Zerkle[7], Patricia Sánchez-Baracaldo[3], Andreas Kappler[1,8], Casey Bryce[9*]

Affiliations:

[1]Geomicrobiology, University of Tübingen, Tübingen, Germany

[2] Hydrogeology, University of Tübingen, Tübingen, Germany

[3] School of Geographical Sciences, University of Bristol, Bristol, UK

[4] Department of Earth System Science, Stanford University, Stanford, USA

[5] School of Life Sciences, Arizona State University, Tempe, AZ, USA.

[6] Department of Earth & Atmospheric Sciences, University of Alberta, Edmonton, Canada

[7] School of Earth & Environmental Sciences and Centre for Exoplanet Science, University of St Andrews, St Andrews, UK

[8] Cluster of Excellence: EXC 2124: Controlling Microbes to Fight Infections, Tübingen, Germany

[9] School of Earth Sciences, University of Bristol, Bristol, UK

*Correspondence:

Dr Casey Bryce, School of Earth Sciences, Wills Memorial Building, Queens Road Bristol, BS8 1RJ

Email: casey.bryce@bristol.ac.uk

Abstract:

Anoxygenic phototrophic Fe(II)-oxidizers (photoferrotrophs) are thought to have thrived in Earth's ancient ferruginous oceans and played a primary role in the precipitation of Archean and Paleoproterozoic (3.8-1.85 Ga) banded iron formations (BIF). The end of BIF deposition by photoferrotrophs has often been interpreted as being the result a deepening of water column oxygenation below the photic zone concomitant with the proliferation of cyanobacteria. We suggest here that a potentially overlooked aspect influencing BIF precipitation by photoferrotrophs is competition with another anaerobic Fe(II)-oxidizing metabolism. It is speculated that microorganisms capable of coupling Fe(II) oxidation to the reduction of nitrate were also present early in Earth history when BIF were being deposited, but the extent to which they could compete with photoferrotrophs when favourable geochemical conditions overlapped is unknown. Utilizing microbial incubations and numerical modelling, we show that nitrate-reducing Fe(II)-oxidizers metabolically outcompete photoferrotrophs for dissolved Fe(II). Moreover, the nitrate-reducing Fe(II)-oxidizers inhibit photoferrotrophy via the production of toxic nitric oxide (NO). Four different photoferrotrophs, representing both green sulfur and purple non-sulfur bacteria, are susceptible to this toxic effect despite having genomic capabilities for NO detoxification. Indeed, despite NO detoxification mechanisms being ubiquitous in some groups of phototrophs at the genomic level (e.g. *Chlorobi and Cyanobacteria*) it is likely they would still be influenced by NO stress. We suggest that the production of NO during nitrate-reducing Fe(II) oxidation in ferruginous environments represents an as yet unreported control on the activity of photoferrotrophs in the ancient oceans and thus the mechanisms driving precipitation of BIF.

INTRODUCTION

Anoxygenic photoautotrophic Fe(II)-oxidizing bacteria, or "photoferrotrophs" (Equation 1), are thought to have thrived in Earth's oceans prior to the rise of O_2 and contributed to the deposition of banded iron formations (Hartman, 1984; Widdel *et al.*, 1993; Konhauser *et al.*, 2002). As O_2 began to rise, these microbes would have seen their habitats shrink, yet they are still thought to have been capable of out-competing abiotic Fe(II) oxidation by O_2 or respiration by microaerophilic Fe(II)-oxidizers while the oxycline remained in the photic zone (Kappler *et al.*, 2005), i.e., when photons could reach deeper anoxic waters.

$$HCO_3^- + 4Fe^{2+} + 10H_2O \overset{h\nu}{\rightarrow} \langle CH_2O \rangle + 4Fe(OH)_3 + 7H^+ \quad (1)$$

However, the rise of O_2 would also have shifted the balance of other biogeochemical cycles towards more oxidized states. Specifically, an increased abundance of nitrate led to pervasive denitrification in stratified water columns during the Great Oxidation Event (GOE) (Zerkle *et al.*, 2017) that began ca. 2.45 Ga. Even prior to the GOE, evidence exists for transient, localized cycling of oxidized nitrogen species associated with areas of locally elevated O_2 (oxygen oases) as early as 2.7 Ga (Busigny *et al.*, 2013), although there is some debate regarding whether the $\delta^{15}N$ record could reflect other N cycling processes independent of oxidative N cycling prior to 2.3 Ga (Garvin *et al.*, 2009; Godfrey and Falkowski, 2009; Busigny *et al.*, 2013; Zerkle *et al.*, 2017; Mettam *et al.*, 2019). NO_x input from atmospheric photochemical reactions would also have supplied oxidized N species to the oceans as far back as the Hadean (Mancinelli and McKay, 1988; Summers and Khare, 2007; Wong *et al.*, 2017).

In modern anoxic environments containing both Fe(II) and nitrate (NO_3^-), nitrate reduction coupled to Fe(II) oxidation (Equation 2) is widespread (Bryce *et al.*, 2018). During this process, Fe(II) oxidation can be enzymatically driven (Straub *et al.*, 1996; He *et al.*, 2016) and/or occur

abiotically (Klueglein and Kappler, 2013), catalyzed by reactive N-intermediates produced during enzymatic reduction of nitrate, such as nitrite and nitric oxide (NO) (known as chemodenitrification) (Klueglein and Kappler, 2013). In modern environments, such as sediments (Melton *et al.*, 2012, 2014; Laufer *et al.*, 2016; Otte *et al.*, 2018) and stratified water columns (Michiels *et al.*, 2017), both nitrate-reducing and phototrophic Fe(II)-oxidizers have been found together. Oxidation of Fe(II) coupled to nitrate reduction could, therefore, compete with photoferrotrophs for Fe(II) in regions where nitrate and light were available but O_2 was absent.

$$10Fe^{2+} + 2NO_3^- + 24H_2O \rightarrow 10Fe(OH)_3 + N_2 + 18H^+ \quad (2)$$

Nitric oxide produced during nitrate-dependent Fe(II) oxidation inhibits photoferrotrophy

In order to observe potential competitive interactions we co-cultured model strains of nitrate-reducing and phototrophic Fe(II)-oxidizing bacteria (enrichment culture KS and *Rhodobacter ferrooxidans* SW2, respectively) and compared cell growth, Fe(II) oxidation, nitrate reduction and nitrous oxide (N_2O) formation in the mixed culture to those grown alone. When the photoferrotroph *R. ferrooxidans* SW2 was incubated alone with 1 mM NO_3^- and 10 mM Fe(II) in the presence of light, Fe(II) oxidation was complete after 28 days and NO_3^- was not consumed (Figure 1a & 1b). The KS culture incubated under the same conditions reduced all available NO_3^- (1 mM) over approximately 4 days and oxidized 5 mM Fe(II), as would be expected from the 5:1 stoichiometry of the reaction (Figure 1a & 1b; Equation 2). When KS and *R. ferrooxidans* SW2 were incubated together, NO_3^- was completely reduced, but Fe(II) oxidation stopped after consumption of approximately 5 mM Fe(II) (Figure 1a & 1b). The remaining 5 mM Fe(II) were not consumed, suggesting inhibition of the photoferrotroph in the presence of the nitrate-reducer KS. Inhibition of *R. ferrooxidans* SW2 was reflected in cell numbers (Figure 1c). A maximum of 10^8 cells/ml were

measured when *R. ferrooxidans* SW2 was incubated alone. Conversely, when incubated in the presence of KS, total cell counts were one order of magnitude lower. The patterns of nitrate reduction, cell growth and Fe(II) oxidation were almost identical in the mixed culture and when KS was incubated alone, with similar trends also observed at lower NO_3^- concentrations (Figure S1). Indeed, the KS and mixed KS - R. *ferrooxidans* SW2 incubations were so similar that Moessbauer spectra of the minerals formed are indistinguishable (Figure S2). These mineralogical analyses also confirm that complete Fe(II) oxidation occurred when R. *ferrooxidans* SW2 was incubated alone, yielding (poorly crystalline) Fe(III) minerals. Conversely both the KS and KS - R. *ferrooxidans* SW2 mixed incubation contained a mix of Fe(II) and Fe(III) minerals, reflecting partial Fe(II) oxidation, as predicted by the stoichiometry of the nitrate-reducing Fe(II)-oxidizing reaction.

The KS culture was previously reported to conduct complete denitrification and produce N_2 as the final product (He *et al.*, 2016; Tominski *et al.*, 2018). Whilst most of the added nitrate in our experiment was ultimately transformed to N_2, concentrations of the denitrification intermediate N_2O increased during nitrate reduction and plateaued after day 6 in both the KS and KS - R. *ferrooxidans* SW2 incubation (with a slight subsequent dilution due to ongoing sampling) (Figure 1f). A parallel incubation inoculated only with KS, and conducted under the same conditions, was needed for separate NO quantification. Therein, we observed that NO was produced (in addition to N_2O) shortly after the onset of the experiment, and persisted in the system over several days, albeit at nM aqueous concentrations, before being consumed (Figure 1d & 1e). Since NO is a potential toxin, we hypothesized that this gaseous intermediate could be driving the observed inhibitory effect (Saraiva *et al.*, 2004).

We employed our mathematical model to assess the importance of NO due to limitations on working with NO in the laboratory. Despite NO being quantified separately from all other chemical

species shown in Figure 1, our model accurately predicted the timing and extent of NO accumulation, and was in good agreement with the measured concentration dynamics of all other species (Figure 1d & 1e). A comparison of measured and modelled Fe(II) oxidation and total biomass growth in a mixed R. *ferrooxidans* SW2 and KS incubation is shown in Figure 2. When NO toxicity was accounted for as an inhibitor of reaction rates in our model, we accurately captured the measured growth and Fe(II) dynamics. When this was not accounted for, the model over-estimated both biomass growth and the extent of Fe(II) oxidation.

The inclusion of toxic inhibition as a function of prolonged exposure to NO (on the order of days) also successfully captured the stalled consumption of N_2O by the KS culture (Figure 1e & 1f). This suggests that components of the KS culture were also, to some extent, influenced by NO accumulation, which then led to stalled N_2O consumption after NO exposure.

We confirmed that a gaseous N-intermediate produced by KS was responsible for inhibiting photoferrotrophy by conducting an additional experiment where the headspace of the reactor was flushed after every sampling point. Although we did not measure N_2O or NO after this headspace exchange, the flushing of the headspace led to uninhibited growth in the mixed culture (Figure 3). N_2O is also a potential toxin (Drummond and Matthews, 1994), therefore we directly tested whether N_2O could inhibit Fe(II) oxidation by R. *ferrooxidans* SW2, but did not observe any inhibition, even at concentrations higher than those observed in Figure 1 (up to 90 µM $N_2O_{(aq)}$) (Figure S3). Our simulation and cultivation results combined confirm that inhibition of *R. ferrooxidans* SW2 is due to prolonged exposure to low levels of NO produced by culture KS.

NO is produced in culture KS because the culture's Fe(II)-oxidizing *Gallionellaceae* sp. only has genes for the first two steps in the denitrification pathway (*nar, nir*) and can, therefore, only reduce nitrate as far as NO (He *et al.*, 2016). The flanking community, consisting mainly of a

Bradyrhizobium sp. (Tominski *et al.*, 2018), contain genes for complete denitrification and were thought to scavenge NO and N_2O in order to complete denitrification. However, we observed that both NO and N_2O accumulated in the KS-inoculated reactors. Our model suggests that the NO accumulation inhibits further denitrification after prolonged NO exposure (~3.5 days) and explains why N_2O is not subsequently consumed. This implies that components of the KS culture (e.g. the flanking community) are not immune to NO toxicity under these conditions. It should be noted that the exposure time-based toxicity function (see section "Reaction Model", Equation 10), was derived from the KS-only incubation and also applied to both KS- and photoferrotroph-catalyzed rates.

Additionally, we evaluated whether inhibition required live and actively metabolizing KS cells, by comparing Fe(II) oxidation in the mixed culture when either live or dead (i.e., autoclaved) KS cells were added (Figure S4). We also added spent, filtered culture KS supernatant to an *R. ferrooxidans* SW2 culture to test whether the inhibitor had been introduced during inoculation (Figure S4). Combined, these experiments demonstrated that the KS culture needed to be alive and actively reducing NO_3^- for inhibition to occur, thus further highlighting that production of the reactive intermediate NO drives the inhibition of the photoferrotroph.

Abiotic and biotic Fe-driven NO production cause photoferrotroph inhibition

If the inhibition effect observed in the KS - *R. ferrooxidans* SW2 co-culture is caused by the production of NO as we suggest, the effect would not be unique to culture KS but would also be observed in other reactions between Fe(II) and nitrogen species. In a further experiment, we observed that inhibition also occurred with the nitrate-reducing Fe(II)-oxidizer *Acidovorax* sp. BoFeN1. This strain reduces nitrate via oxidation of organic carbon. The coupled reaction produces nitrite, which abiotically oxidizes Fe(II) (Figure S5), although the potential for some enzymatic

component to Fe(II) oxidation has not been ruled out. The abiotic reaction between nitrite and Fe(II) produces NO and N_2O in a process known as chemodenitrification (Equation 3 - 5; Klueglein *et al.*, 2014). Nitrite accumulation by *Acidovorax* sp. BoFeN1 is typically in the 1 - 3 mM range under these conditions (Klueglein *et al.*, 2014) whereas culture KS typically only sees nitrite accumulation up to tens of µM, if at all (Tominski *et al.*, 2018).

$$NO_2 + 2Fe^{2+} + 2H^+ \rightarrow 2Fe^{3+} + NO + H_2O \quad (3)$$

$$NO + Fe^{2+} + H^+ \rightarrow Fe^{3+} + HNO \quad (4)$$

$$2HNO \rightarrow N_2O + H_2O \quad (5)$$

We further evaluated whether nitrite itself showed a toxic effect when added to an *R. ferrooxidans* SW2 culture under ferruginous conditions, and observed no Fe(II) oxidation by *R. ferrooxidans* SW2 at 10 µM or 20 µM nitrite (Figure S6). However, in the absence of Fe(II), and with acetate as the electron donor, *R. ferrooxidans* SW2 tolerated nitrite concentrations above 500 µM (Figure S7). This strongly suggests that the abiotic reaction of nitrite and Fe(II), which yields NO as an intermediate (Kampschreur *et al.*, 2011), drives the observed toxicity in these experiments, not nitrite itself which can be tolerated at much higher concentrations in the absence of Fe(II).

Collectively, these experiments demonstrate that three independent mechanisms of nitrate-reducing Fe(II) oxidation (enzymatic Fe(II) oxidation by culture KS, microbially catalyzed chemodenitrification by *Acidovorax* sp. BoFeN1, and entirely abiotic Fe(II) oxidation with nitrite) lead to inhibition of the photoferrotroph *R. ferrooxidans* SW2. In all cases the inhibition can be explained by the production of highly toxic NO as an intermediate of denitrification in ferruginous conditions (Figure 4).

NO detoxification capability is widespread in phototrophs but inadequate to avoid inhibition

The inhibition effect we report here is not unique to *R. ferrooxidans* SW2. We additionally tested whether inhibition of Fe(II) oxidation would occur when an alternative freshwater photoferrotroph, *Chlorobium ferrooxidans* strain KoFox, was incubated with culture KS. In this case, Fe(II) oxidation was delayed but not completely inhibited (Figure S8). We also observed that two marine photoferrotrophs (*Chlorobium sp.* N1 and *Rhodovulum rubiginosum*) were sensitive to chemodentification processes in the presence of Fe(II). *Chlorobium* sp. N1 oxidized Fe(II) with 2 µM and 10 µM nitrite added (to promote NO formation via abiotic reaction with Fe(II)), but not with 20 µM nitrite. *R. rubiginosum* oxidized Fe(II) with 2 µM nitrite, but not with 10 µM or 20 µM (Figure S6). The Fe(II) oxidation mechanism in this case is of the type depicted in Figure 4c. Sensitivity of these marine strains highlights that we also expect to observe a similar effect in the marine realm. Interestingly, for both the freshwater and marine strains, the green sulfur bacteria tested appeared to tolerate slightly higher nitrite concentrations than the purple non-sulfur bacteria tested, in turn, suggesting a higher tolerance to NO. This may be the result of physiological differences between the green sulfur and purple non-sulfur bacteria, or it could be because both green sulfur bacteria strains do not exist in pure culture and thus may be "helped" by a partner strain.

All of the strains tested have some genetic capability to tolerate NO. *Chlorobium ferrooxidans* sp. KoFox, *Chlorobium* sp. N1 and *Rhodovulum robiginosum* all possess the *norV* gene, a flavorubredoxin which reduces NO for detoxification purposes (Gardner *et al.*, 2002). Conversely, *Rhodobacter ferrooxidans* SW2 contains the *norB* gene encoding the canonical NO reductase in the denitrification pathway (*cNor*). However, it is more likely *cNor* has a detoxification role in this strain which is incapable of denitrification (as demonstrated in Figure 1). This suggests either that the possession of NO reduction genes, regardless of type, does not accurately predict a strain's ability to tolerate NO, or that the concentrations of NO produced in our experiments are

outside the range in which NO can be efficiently detoxified. This hypothesis is supported by the fact that our experiments and simulations suggest that NO toxicity is also responsible for the stalled N_2O reduction observed in the KS culture itself, in which the partner strains have NO-reducing capabilities (Blöthe and Roden, 2009; He *et al.*, 2016).

In order to visualize how genetic capabilities for NO detoxification in our cultured phototrophs compared to other phototrophic bacteria, we implemented comparative genomic analysis to map the presence of *norV*, *norB* or *hmpA* (a two-domain flavohemoglobin also known to convert NO to nitrate; Gardner et al., 1998) across all available phototroph genomes in the NCBI RefSeq database. Phototrophs were identified based on photosynthetic marker genes encoding for cyanobacterial photosystem I (*psaB*) and II (*psbA*) and non-cyanobacterial type I and type II reaction centres (*pshA* and *pufL* respectively). Marker genes for NO reduction are widespread within the phototroph genomes: 53 (7%) have *hmpA*, 314 (41%) have *norV* and 129 (17%) have *norB* (Figure 5). Anoxygenic phototrophs with type I reaction centres (i.e., the *Chlorobi*) and *Cyanobacteria* almost all contain *norV* (98% of *Cyanobacteria*, n = 259; 92% of *Chlorobi*, n = 22) and none contain *hmpA*. None of the *Chlorobi* have *norB* genes whilst a small number of *Cyanobacteria* (28, 11%) do. *norV* is much less common in anoxygenic phototrophs with type II reaction centres (i.e., purple bacteria), as it is only present in 36 species (8%), however *norB* (102, 21%) and *hmpA* (53, 11%) genes are more common.

Our results suggest that there are differences in genetic strategies for NO detoxification amongst different groups of phototrophs and emphasize that our cultured photoferrotrophs (Supplementary Figure S9) are broadly representative of their respective groups. Although comparative genomics only show whether the genes identified are present in phototrophs, more analyses would be needed to test under which condition these genes are expressed. However, the broad genomic sampling (Figure 5) implies that the inhibition we observe in culture is likely not

limited to our tested strains but that all phototrophs may be vulnerable despite having some genetic ability to detoxify NO. Additionally, the ubiquity of *norV* amongst the genomes of extant *Cyanobacteria* and *Chlorobi spp.* suggests this gene may have evolved early in the history of these groups.

Would inhibition by NO be expected in modern and ancient environments?

Measured NO concentrations in modern ferruginous systems are highly variable but can reach up to 500 nM e.g. in anoxic sediments (Schreiber *et al.*, 2008, 2014). In these settings NO may be produced as a by-product of microbial denitrification or chemodenitrification, but is also an intermediate of nitrification and ammonium oxidation (Kuypers *et al.*, 2018). We demonstrated that NO concentrations during KS-mediated denitrification can accumulate to levels of up to 15 nM (Figure 1), which is about 30-fold lower than the highest concentrations measured in some modern anoxic settings, thus NO sensitivity could be expected at environmentally relevant concentrations.

The Fe(II) concentrations used in this study are high compared to modern environments and are at the very upper end of estimates for Archean (Thompson et al., 2019) and Proterozoic ferruginous oceans (Derry, 2015; Stanton *et al.*, 2018), although in reality seawater Fe(II) concentrations at the time of BIF deposition were likely lower (up to 0.5 mM; Morris, 1993). The nitrate concentrations are also higher than would be expected in both modern and ancient settings. The archean ocean is thought to have contained < 1μM NO_3^- (Ranjan *et al.*, 2019) whereas modern surface NO_3^- concentrations range from e.g. 25 µM to < 0.1 µM in the Indian Ocean or 8 µM to < 0.1 µM in the equatorial Pacific (Altabet and Francois, 1994). However, it must be considered that measured natural NO_3^- concentrations are highly variable and often low because they reflect high N turnover and not low NO_3^- availability. Indeed, Archean NO_3^- concentrations are estimated to be

low precisely because of reaction between nitrogen oxides and ferrous iron, which produces short-lived reactive N species such as NO.

It is important to stress that the high Fe(II) (10 mM) and NO_3^- (0.4 and 1 mM) concentrations used here were a practical necessity to quantify the co-culture dynamics experimentally as the Fe(II):NO_3^- ratio has to be set such that there is enough NO_3^- to observe Fe(II) oxidation by culture KS, but not so much as to leave no remaining Fe(II) for the photoferrotroph. 0.4 mM nitrate is the lowest concentration we could use whilst still being able to clearly measure the Fe(II) oxidation. However, our concentrations are in line with similar experimental studies (Stanton *et al.*, 2018; Thompson *et al.*, 2019). Because NO is the driving force of inhibition it is unlikely that the excess of Fe(II) has a significant effect on whether or not inhibition occurs. Moreover, we observe that concentrations as low as 15 nM NO have the ability to hinder the growth of phototrophs. Therefore, we expect that environmentally realistic NO concentrations can exert a strong selective pressure on the microbial community in modern ferruginous environments such as sediments, oxygen minimum zones and ferruginous, stratified lakes.

Ferruginous environments were much more common in the Earth's past and thus the effects we report here were likely more important earlier in Earth's history. The complete biological cycle of nitrogen fixation, nitrification and denitrification (including chemodenitrification) had likely evolved by the late Archean or early Proterozoic (Garvin *et al.*, 2009; Godfrey and Falkowski, 2009; Stüeken *et al.*, 2016; Stanton *et al.*, 2018), although it is thought that up to 10^{13} g per year of NO could have been produced by atmospheric photochemical reactions as far back as the Hadean (Wang *et al.*, 1998). The existence of microbially driven nitrate-reducing Fe(II) oxidation - which linked the Fe and C biogeochemical cycles - has been evoked to explain the inverse co-variations between $\delta^{15}N$ and $\delta^{13}C$ isotopes recorded in the early Paleoproterozoic Brockman Iron Formation in Western Australia (Busigny *et al.*, 2013). In an alternative scenario, these authors propose that

Fe-driven chemodenitrification in a redox-stratified water column could drive the observed signatures. Our results demonstrate that nitrate-reducing Fe(II) oxidation would have the potential to inhibit the activity of photoferrotrophs in systems similar to those which produced the Brockman IF. Considering that photoferrotrophs are thought to have contributed to BIF formation as early as 3.77 Ga (Czaja *et al.*, 2013; Pecoits *et al.*, 2015), and nitrate was likely at least locally available as early as 2.7 Ga (Godfrey and Falkowski, 2009), there is a potentially long time frame from then until the onset of the GOE (2.45 Ga) within which photoferrotrophs could have encountered microbial or abiotic nitrate-reducing Fe(II) oxidation in the photic zone. Based on the ubiquity of photoferrotrophs for which NO is toxic, our findings imply, at the very least, that nitrate-reducing Fe(II) oxidation could have imposed a selection pressure on strains with detoxifying capabilities or provided an impetus to evolve NO detoxifying traits. At worst, nitrate-reducing Fe(II) oxidation could have created photoferrotroph exclusion zones in regions with elevated nitrate availability.

Whilst our study has focused on the effect of nitrate-reducing Fe(II) oxidation on anoxygenic phototrophs, other microbial lineages could also be affected by NO accumulation under ferruginous conditions. Indeed previous authors have noted that early accumulation of NO via photochemical reactions in the atmosphere would have provided one of the most promising electron acceptors for early life (Ducluzeau *et al.*, 2009; Wong *et al.*, 2017; Hu *et al.*, 2019). It is even considered likely that NO and O_2 reductases share an evolutionary history (Saraste and Castresana, 1994; Chen and Strous, 2013). Local accumulation of NO in the early oceans has also been proposed to have led to antagonistic interactions between denitrifying (e.g., NO-producing) bacteria and cyanobacteria (Santana *et al.*, 2017). Those authors even go so far as to suggest that NO toxicity would represent the first cyanobacterial “disease” which gave rise to NO defense mechanisms in cyanobacteria and laid the groundwork for the evolution of phytopathogenesis. The ubiquity of NO detoxification

genes we observe in the *Chlorobi* and Cyanobacteria may hint towards this shared stress early in each group's evolutionary history.

The potential marginalization of photoferrotrophs by nitrate-reducing Fe(II)-oxidizers represents a previously unknown control on mechanisms of BIF deposition. As the marine photic zone became progressively oxygenated prior to the GOE, one of the immediate outcomes would have been the production of nitrate in marine settings with high primary productivity. This would have been followed by the proliferation of either chemodenitrification or enzymatic denitrification, with the two processes influencing photoferrotrophs via metabolic competition for Fe(II) as the electron donor, production of NO as a toxin, or a combination of the two.

In terms of BIF deposition, we envisage an Archean ocean where photoferrotrophs were the primary biological driver of Fe(II) oxidation in the photic zone. However, as nitrate became more abundant and denitrification intensified, the photoferrotrophs would have been pushed further offshore, away from areas of peak primary productivity where cyanobacteria grew as mats (Blank and Sánchez-Baracaldo, 2010; Sánchez-Baracaldo, 2015), and where O_2 and oxidized N species were accumulating. Although the photoferrotrophs would still have had first access to upwelling Fe(II) (Kappler *et al.*, 2005; Jones *et al.*, 2015), they would have found themselves limited by other trace elements sourced from continental weathering. Furthermore, as O_2 increasingly diffused away from coastal environments the oxic zone would have eventually intersected the photic zone. As photoferrotrophs are obligate anaerobes, this oxygen would have completely limited their ability to survive in the open oceans. Consequently, upwelling Fe(II) would no longer have been oxidized via photoferrotrophy. At this stage, Fe(II) oxidation would instead have been driven by microaerophilic chemolithoautotrophs (e.g., *Gallionella*), nitrate-reducing Fe(II)-oxidizers, or abiotic Fe(II) oxidation with oxygen or reactive nitrogen species.

If photoferrotrophs were inhibited, how much BIF deposition could be driven by nitrate-reducing Fe(II) oxidation alone? It has been previously hypothesized that the inverse correlation between $\delta^{15}N$ and $\delta^{13}C_{carb}$ values in the Palaeoproteozoic Brockman IF could be explained by partial denitrification by nitrate-reducing Fe(II)-oxidizing bacteria, with the nitrate sourced from nitrification (oxidation of NH_4^+) in a stratified water column (Busigny *et al.*, 2013). It is estimated that deposition of the 2.48 Ga Dales Gorge Member of the Brockman Iron Formation required peak Fe(II) oxidation rates of 7.85×10^{11} mol of Fe per year (Konhauser *et al.*, 2018). Thus, given the stoichiometry of nitrate:Fe(II) in the nitrate-reducing Fe(II)-oxidizing reaction (5:1; Equation 2), reduction of 1.57 x 10^{11} mol of nitrate per year would be required to oxidize all of this iron. Primary productivity in the Archean and Paleoproterozoic could have been as low as 10% of modern levels (Canfield *et al.*, 2010), with a further 50% decrease in N_2 fixation rates due to Mo limitation of nitrogenase enzymes (Zerkle *et al.*, 2006), yielding an estimated nitrogen fixation rate of 5 x 10^{11} mol/year. 31% of this fixed nitrogen would need to be oxidized to provide enough nitrate to form adequate amounts of BIF from nitrate-dependent Fe(II) oxidation, assuming no nitrate loss via heterotrophic denitrification or anaerobic ammonium oxidation. Given that there is no persistent signal for heterotrophic denitrification or anammox in the $\delta^{15}N$ record until ~2.3 Ga (Zerkle *et al.*, 2017), and that Fe^{2+} could have been a much more widely available electron donor in deep ferruginous oceans than organic matter, we find this to be a plausible assumption. These estimates of N availability do not account for abiotic sources of fixed N such as lightning, volcanism, and bolide impacts which could collectively account for N fluxes of the same magnitude as biological N fixation (~ 2.5 x 10^^{11} mol N yr^{-1}) (Kasting, 1990; Mather *et al.*, 2004; Harman *et al.*, 2018) and would make the potential for nitrate-dependent Fe(II) oxidation even more widespread. Therefore, we hypothesize that it was possible that nitrate-reducing Fe(II) oxidation could have compensated to a significant extent for BIF deposition after photoferrotrophs became inhibited. While nitrate-

reducing Fe(II)-oxidizers might initially have compensated for the lack of BIF deposition by photoferrotrophs, the aerial expansion of cyanobacteria and oxygenation of the deep ocean would ultimately have resulted in the cessation of BIF deposition.

Conclusions

Our work represents the first experimental evidence that NO produced by denitrifying bacteria can influence the survival of photoferrotrophs, and highlights that this toxicity would be enhanced under ferruginous conditions. The levels of NO required to inhibit photoferrotrophy are low and within the range observed in modern ferruginous environments, suggesting that NO stress could have played an important role in shaping the biogeochemistry and microbial community in both modern and ancient ferruginous habitats with an active N cycle. It is often thought that the main challenge for photoferrotrophs arose when O_2 became more widespread. However, the introduction of reactive nitrogen species, such as NO_2^- and NO into a ferruginous world would also have made photoferrotrophy difficult. Local enrichment of NO may have influenced biogeochemical cycling and, via competition with mineral precipitating phototrophs, fundamentally altered the mechanisms of BIF deposition, one of the main records of early ocean biogeochemistry itself.

METHODS

Model strains

All experiments described in the main text were conducted with the autotrophic nitrate reducing Fe(II)-oxidizing enrichment culture KS (Straub *et al.*, 1996) and the phototrophic Fe(II)-oxidizer *Rhodobacter ferrooxidans* SW2 (Ehrenreich and Widdel, 1994). Culture KS was enriched from a ditch in Bremen, Germany and SW2 was isolated from freshwater sediments in Hannover,

Germany. Both cultures were maintained in continuous culture in the culture collection of Andreas Kappler. Media recipes for other strains used can be found in Table S1.

Cultivation

For cultivation of KS and *R. ferrooxidans* SW2 22 mM bicarbonate-buffered mineral media was used for all set ups and contained: 0.6 g/L KH_2PO_4, 0.3 g/L NH_4Cl, 0.025 g/L $MgSO_4 \cdot 7\ H_2O$, 0.4 g/L $MgCl_2 \cdot 6\ H_2O$, 0.1 g/L $CaCl_2 \cdot 2\ H_2O$. After autoclaving in a Widdel flask the media was cooled to room temperature under an N_2/CO_2 atmosphere (90:10) and buffered with anoxic 22 mM bicarbonate buffer. Aliquots of 1 mL L^{-1} sterile filtered 7-vitamin solution (Widdel and Pfenning, 1981), trace element solution (Widdel et al., 1983) and selenite-tungstate solution (Widdel and Bak, 1992) were added and the pH was adjusted to 7 with 0.5 M $NaHCO_3$ or 1 M HCl. Media was stored at 5 °C. Before each experiment, the media was aliquoted into sterile glass serum vials with a 50 % headspace consisting of N_2/CO_2 gas (90:10) and amended with $FeCl_2 \cdot 4H_2O$ and $NaNO_3$ as required. The initial cell density of each strain was approximately 10^6 cells/mL unless stated otherwise and the pre-culture was always grown under Fe(II)-oxidizing conditions. Serum vials were placed in a light incubator with 24h light that reached 23 ± 3 µmol/m^2/s (2,700 K) at 25 °C. Vial position was randomized after each sampling point to avoid enhancing any effects caused by incubator position. Media recipes for the other strains tested (*Acidovorax* sp. BoFeN1, *Chlorobium* sp. N1, *Rhodovulum rubiginosum*) can be found in Table S1.

Competition between KS and SW2

To evaluate potential competitive effects between KS and *R. ferrooxidans* SW2, 50 mL media was amended with 10 mM $FeCl_2$ and 0.4 mM (scenario A) or 1 mM $NaNO_3^-$ (scenario B). These

concentrations are high compared to what is expected in modern or ancient environments but is a practical necessity in order to monitor the competitive dynamics. Three different conditions were tested: KS alone, *R. ferrooxidans* SW2 alone, and KS and *R. ferrooxidans* SW2 grown together in the same vial. At every sampling time point samples for gas analyses was performed under sterile conditions at the lab bench before samples for Fe, NO_2^-, NO_3^-, and cells were taken in a glovebox under an N_2 atmosphere.

Further control experiments

The potential for inhibition by the presence of KS biomass or a component from the supernatant was evaluated. For this we repeated the experiment but inoculated additional triplicates with cells from an autoclaved pre-culture (121 °C, 20 mins) or with an equal volume of pre-culture supernatant that had been passed through a 0.22 µm filter. Samples for Fe, NO_2^-, NO_3^-, N_2O and cell number were collected at every time point as described in the previous section.

Toxicity tests

To determine whether potentially toxic gaseous products were causing inhibition of *R. ferrooxidans* SW2 when grown in combination with KS, we prepared six vials as described in the experiment above with 10 mM $FeCl_2$ and 1 mM $NaNO_3^-$. Three vials were flushed with an N_2/CO_2 gas mix for 5 minutes after every sampling time point or every other day. The remaining three vials did not have the headspace replenished at any point.

The potential for N_2O toxicity in strain *R. ferrooxidans* SW2 was tested by inoculation into different concentrations of N_2O with 10 mM $FeCl_2$ as electron donor. These tests were performed in 15 mL Hungate tubes with 9 mL media and 1 mL inoculum in triplicates. Growth was monitored

visually with positive growth demonstrated by a colour change from grey to orange. The concentration range was from 0 µM $N_2O_{(aq)}$ to 90 µM N_2O (0, 9, 18, 45 and 90 µM $N_2O_{(aq)}$).

Different concentrations of NO_2^- (0, 2, 10, 20 µM) were tested in combination with 10 mM $FeCl_2$, in duplicates, to determine the potential for nitrite toxicity. Microbial Fe(II) oxidation was indicated by a colour change from grey to orange. NO_2^- toxicity was tested for 4 phototrophic Fe(II)-oxidizers in total: *Rhodobacter ferrooxidans* SW2, *Rhodovulum rubiginosum*, *Chlorobium* sp. strain N1 and *Chlorobium ferrooxidans* strain KoFox (please see SI for culture conditions for additional strains). Toxicity of NO_2^- in the absence of Fe(II) was determined by incubating *Rhodobacter ferrooxidans* SW2 with acetate as an alternative growth substrate. Growth was monitored using optical density at 660 nm in the presence of either 0 mM, 0.5 mM or 2 mM $NaNO_2^-$.

Iron quantification

Iron (Fe(II) and Fe(III)) was quantified spectrophotometrically with the ferrozine assay after Stookey (1970). Due to the potential presence of nitrite the protocol was modified and 1 M HCl was used together with 40 mM sulfamic acid (Schaedler et al. 2018, Klueglein et al. 2013) to stabilize iron from abiotic reactions with nitrogen species. During sampling, 0.1 mL of sample was added to 0.9 mL 40 mM SA in 1 M HCl. Samples were stored at 5 °C until quantification. The ferrozine-Fe(II) complex was quantified at 562 nm using a microtiter plate reader (Multiskan GO, Thermo Fisher Scientific). Ferrozine measurements were conducted in triplicates.

Cell quantification

Cells were counted using a flow cytometer equipped with a 488 nm laser as an excitation source (Attune Nxt flow cytometer, Thermo Fisher Scientific). Samples for cell counts were directly processed after sampling. 600 µL of sterile filtered oxalate solution were added to 200 µL of sample and incubated for 30 sec to 1 min. 1200 µL 10 mM sterile filtered bicarbonate buffer was added, and the mixture centrifuged at 15000 rpm for 10 min. 1800 µL of the supernatant was discarded and 600 µL 10 mM sterile filtered bicarbonate buffer was added. BacLight Green stain (Thermo Fisher Scientific, 1µl stain/1 ml sample) was added and 200 µL of sample was distributed in triplicates in 96 well plates. The plate was incubated for 15 minutes in the dark before measuring. Cells were distinguished from noise or debris based on their properties in the side scatter and BL1 channel (with emission filter 530/30 nm). This method measures total cell numbers and does not distinguish between different species.

N_2O quantification: Samples were extracted from the headspace using a Hamilton syringe after each bottle was shaken and transferred into vials previously flushed with N_2. The vials were stored at room temperature until further analysis. The analysis was performed by a Gas Chromatograph with a Pulsed Discharged Detector (PDD). The temperature program for the columns was: 10 minutes at 35 °C, 50 °C per minute until 120 °C, 120 °C for one minute. This was repeated with 50 °C per minute until 150 °C and left for 5 min. The valve furnace was set to 40 °C. The carrier gas was run at 5 mL/min and run time was 18.3 min. Back PDD used was Molsieb5a 30mx0.53 and front PDD was TG BondQ+ 30mx0.25. Injection volume was 2 mL.

NO_2^- and NO_3^- quantification

Samples for NO_2^- and NO_3^-, were taken in a glovebox, centrifuged at 13,400 rpm for 5 min, and then stored under anoxic conditions at 5 °C until measurement. Concentrations were quantified colorimetrically using a continuous-flow analyzer (Seal Analytical Norderstedt, Germany). For details see (Tominski *et al.*, 2018).

NO monitoring

To determine if NO accumulated during growth of the KS culture we conducted a parallel incubation with only KS inoculated in the reactor but under the same conditions as in the original experiment. For this incubation, cells pre-grown with Fe(II) as an electron donor were transferred (0.5 % inoculum) into reactors containing fresh media with 10 mM $FeCl_2$, 1 mM $NaNO_3$ and an N_2/CO_2 (90:10) headspace. The cultures were incubated in the dark at 25 °C and NO and N_2O evolution was followed over time. NO was quantified in the microcosm headspace with a chemiluminescence-based analyzer (LMA-3D NO2 analyzer, Unisearch Associates Inc., Concord, Canada). Headspace gas (50 µL) was sampled by replacement under sterile conditions using a CO_2-N_2-flushed gas-tight syringe and injected into the analyzer. The injection port was customized to fit the injection volume and consisted of a T-junction with an air filter at one end and a septum at the other end. An internal pump generated consistent airflow. Our method generally followed a previous protocol (Homyak *et al.*, 2016), and included adjustments based on our experimental set up. In short, NO was oxidized to NO_2 by a CrO_3 catalyst. The NO_2 passed across a fabric wick saturated with a Luminol solution. Luminol was obtained from Drummond Technology Inc. (Bowmanville, Ontario, Canada). Readings were corrected for background NO_2 every 15 minutes. Shell airflow rate was kept at 500 mL min^{-1} and the span potentiometer was set to 8. Measurements

were calibrated with a 0.1 ppm NO (in N_2) standard (<0.0005 ppm NO_2, Scott-Marin, Riverside, CA, USA) over a range of 50–10,000 ppb.

Moessbauer spectroscopy

Samples for ^{57}Fe Moessbauer spectroscopy were prepared inside an anoxic (100 % N_2 atmosphere) glovebox by passing the sample through a 0.45 µm filter and sealing the filter paper between two pieces of airtight Kapton tape. The samples were stored in airtight (100 % N_2 atmosphere) bottles at -20 °C until analysis. The bottles were opened just before loading the samples inside a closed-cycle exchange gas cryostat (Janis cryogenics) under a backflow of helium. Spectra were collected at 77 K with a constant acceleration drive system (WissEL) in transmission geometry with a ^{57}Co/Rh source and calibrated against a 7 µm thick α-^{57}Fe foil measured at room temperature. All spectra were fitted applying a Voight based fitting (VBF) routine (Rancourt and Ping, 1991) using the Recoil software (University of Ottawa). The half width at half maximum (HWHM) was fixed at 0.13 mm s^{-1} for all samples.

Reaction model

Incubation reactors for all experimental treatments, photoferrotrophy by *R. ferrooxidans* SW2, photoferrotrophy and nitrate dependent Fe(II) oxidation (*R. ferrooxidans* SW2 plus KS) and KS-mediated nitrate dependent Fe(II) oxidation, were all simulated as well-mixed batch reactors. The model variants simulate microbially mediated reactions considering Monod kinetics explicitly accounting for biomass.

The growth rate of *R. ferrooxidans* SW2 (r_{SW2}) during photoferrotrophy, in the presence of a continuous light source, was modeled via a single-Monod rate expression (Equation 6):

$$r_{SW2} = \mu_{max}\left(\frac{C_{Fe(II)}}{C_{Fe(II)} + K_{Fe(II)}}\right)X_{SW2} \quad (6)$$

where μ_{max} [day^{-1}] is the maximum specific growth rate constant for photoferrotrophy, $C_{Fe(II)}$ [mM] is the concentration of aqueous Fe(II), $K_{Fe(II)}$ [mM] is the half-saturation constant, and X_{SW2} [cells mL^{-1}] is the biomass density of suspended SW2. The equation for r_{SW2} assumes that light is non-limiting. The corresponding concentration changes of X_{SW2} and Fe(II) with respect to time are given by:

$$\frac{dX_{SW2}}{dt} = r_{sw2} \quad (7)$$

$$\frac{dC_{Fe(II)}}{dt} = -\frac{r_{SW2}}{Y_{SW2}} \quad (8)$$

where Y_{SW2} [cells mmol$_{Fe(II)}^{-1}$] is the growth yield of SW2 on Fe(II).

Nitrate-reducing Fe(II) oxidation by KS was modeled considering each denitrification step ($NO_3^- \xrightarrow{1} NO_2^- \xrightarrow{2} NO \xrightarrow{3} N_2O \xrightarrow{4} N_2$), where electron acceptor (N-species) and electron donor (Fe(II)) dependence was accounted for via dual-Monod kinetics. Although there is abundant discussion in the literature regarding which strain in the enrichment culture is responsible for each denitrification step, and the extent to which each step is enzymatically coupled to Fe(II) oxidation (Blöthe and Roden, 2009; He *et al.*, 2016; Tominski *et al.*, 2018), we opted to adopt the simplest scenario in the simulations which does not distinguish between community members and assumes all denitrification steps are enzymatically coupled to Fe(II) oxidation. The true scenario may be more complex; however, our model formulation successfully captured the dynamics of the culture well, and accurately predicted the timing and magnitude of formation of reactive intermediates.

476 The growth rate of KS, r_{KS}^{i}, during each denitrification step is given by the following
477 generalized expression:

$$r_{KS}^{i} = \mu_{max}^{i}\left(\frac{C_{Fe(II)}}{C_{Fe(II)} + K_{Fe(II)}}\right)\left(\frac{C_{N_i}}{C_{N_i} + K_{N_i}}\right)X_{KS}f_{tox}^{NO} \quad (9)$$

478 where μ_{max}^{i} [day^{-1}] is the maximum specific growth rate constant for the reduction of nitrogen
479 species, *i*, coupled to Fe(II) oxidation, K_{N_i} [mM] is the half-saturation constant for each i^{th} electron
480 acceptor in the denitrification chain and X_{KS} [cells mL^{-1}] is the biomass density of suspended KS.
481 All growth rate expressions were scaled by f_{tox}^{NO} [-], an NO exposure time-based toxicity function
482 ($0 < f_{tox}^{NO} < 1$). Toxicity effects were included based on the observation that NO accumulated at
483 detectable levels in the headspace of the reactors, and that denitrification stopped (in multiple
484 replicated incubations) after 3.5 days. Therefore, we modified a concentration-based toxicity
485 function (Belli *et al.*, 2015) to an exposure time formulation, based on the extremely high NO
486 toxicity, even at low concentrations.

$$f_{tox}^{NO} = \frac{1}{1 + \left(\frac{\tau}{\tau_D}\right)^{p}} \quad (10)$$

487 In equation (7), τ [days^{-1}] is the exposure time to NO above a threshold concentration of 10 nM
488 (based on best fit results), τ_D [days^{-1}] exposure time at 50 % inhibition and p [-] is an exponent
489 characterizing the slope of the curve at the τ_D inflection point.

490 Each step in the denitrification chain was modelled as a microbially mediated step, assumed
491 to be carried out by a facet of the KS culture. Abiotic reaction steps were not accounted for in our
492 model formulation.

493 Kinetic mass-transfer between the aqueous and gaseous phases (headspace and liquid) was
494 simulated via a linear-driving force approximation, assuming Henry's law partitioning of NO, N_2O
495 and N_2.

$$r_{tr}^{i} = k_{tr}\left(C_{N_i} - \frac{P_{N_i}}{RTH_i}\right) \quad (11)$$

496 In equation 11, k_{tr} [days^{-1}] is the first-order mass transfer rate coefficient, C_{N_i} [mM] is the aqueous
497 phase concentration, P_{N_i} [Pa] is the partial pressure, H_i [-] is the Henry's law constant of the *i*-th
498 volatile N-compound, respectively, *R* is the ideal gas constant, and *T* is the absolute temperature.
499 Headspace dilution due to sampling was also considered.

500 The aqueous concentration changes for Fe(II), N-species and KS are given by:

$$\frac{dC_{Fe(II)}}{dt} = -\sum_{i=1}^{n}\frac{r_{KS}^{i}}{Y_{KS}} \quad (12)$$

$$\frac{dC_{NO3}}{dt} = -\frac{1}{2}\frac{r_{KS}^{NO3}}{Y_{KS}} \quad (13)$$

$$\frac{dC_{NO2}}{dt} = \frac{1}{2}\frac{r_{KS}^{NO3}}{Y_{KS}} - \frac{1}{2}\frac{r_{KS}^{NO2}}{Y_{KS}} \quad (14)$$

$$\frac{dC_{NO}}{dt} = \frac{r_{KS}^{NO2}}{Y_{KS}} - \frac{r_{KS}^{NO}}{Y_{KS}} - r_{tr}^{NO} \quad (15)$$

$$\frac{dC_{N_2O}}{dt} = \frac{1}{2}\frac{r_{KS}^{NO}}{Y_{KS}} - \frac{1}{2}\frac{r_{KS}^{N_2O}}{Y_{KS}} - r_{tr}^{N_2O} \quad (16)$$

$$\frac{dC_{N_2}}{dt} = \frac{1}{2}\frac{r_{KS}^{N_2O}}{Y_{KS}} - r_{tr}^{N_2O} \quad (17)$$

$$\frac{dX_{KS}}{dt} = \sum_{i=1}^{n} r_{KS}^{i} \quad (18)$$

For the case of a mixed *R. ferrooxidans* SW2 and KS incubation, the growth rate of photoferrotrophy is also inhibited by NO toxicity, hence, the concentration change of iron is given by:

$$\frac{dC_{Fe(II)}}{dt} = -\sum_{i=1}^{n} \frac{r_{KS}^{i}}{Y_{KS}} - r_{SW2} \cdot f_{tox}^{NO} \quad (19)$$

Changes in the partial pressures of NO, N_2O and N_2 are given by:

$$\frac{dP_{NO}}{dt} = -\frac{P_{NO}Q_s}{V_g} + \left(\frac{V_w}{V_g}\right) RT \cdot r_{tr}^{NO} \quad (20)$$

$$\frac{dP_{N_2O}}{dt} = -\frac{P_{N_2O}Q_s}{V_g} + \left(\frac{V_w}{V_g}\right) RT \cdot r_{tr}^{N_2O} \quad (21)$$

$$\frac{dP_{N_2}}{dt} = -\frac{P_{N_2}Q_s}{V_g} + \left(\frac{V_w}{V_g}\right) RT \cdot r_{tr}^{N_2} + pN_2^{atm} \cdot \frac{Q_s}{V_g} \quad (22)$$

Periodic sample collection was simulated as the constant sampling rate, Q_s [L s^{-1}] (based on the total amount of sample volume collected over the duration of the experiment), and assumed to result in headspace dilution of NO, N_2O and N_2 partial pressures, P_{NO}, P_{N_2O}, and P_{N_2}[Pa], respectively. In equations 15 through 17, V_w and V_g are the aqueous and gaseous volumes [L], respectively. An addition of N_2 as a result of headspace volume replacement during sampling is accounted for by the addition of headspace gas at "atmospheric" (80% N_2) partial pressure, pN_2^{atm}. (Note: experiments were run under an anerobic 90:10 N_2:CO_2 atmosphere.)

All model variants were setup as well-mixed batch reactors. Partitioning of NO, N_2O and N_2 between aqueous and gas phases was considered in model variants that simulated nitrate-reducing

iron oxidation. The coupled system of ordinary differential equations was solved in MATLAB using the built-in ordinary differential equation solver, *ode15s*. We fitted both the SW2-only and KS-only models to measured concentration, cell density and partial pressure data using the least squares MATLAB fitting tool, *lsqnonlin*. We fitted the logarithms of the parameters rather than the parameters themselves, thereby alleviating the discrepancy between nominal values differing by orders of magnitude. Our fitting scheme was based on minimizing the sum of squared differences between measurements and simulated output. Additional weight was allocated to NO partial pressure measurements. We justify increasing the importance of those measurements as they represent a key feature in the observed toxicity response of both KS and phototrophs to NO accumulation. Calibrated parameter values for photoferrotrophy and NDFO catalyzed by the KS culture are presented in Table S1.

Bioinformatics

Hundreds of thousands of assembly structure report files were downloaded from the NCBI RefSeq database (O'Leary *et al.*, 2016) to study the distribution of nitric oxide reductase genes in bacterial genomes. This number was reduced to ~30,000 assemblies by selecting only the best assembly for each species (as defined in the NCBI taxonomy database information for the genomes, Schoch *et al.*, 2020). RNAmmer v1.2 was used to obtain SSU rRNA sequences from each genome (Lagesen *et al.*, 2007). Genomes without any 16S sequence were excluded from the analysis, with a final dataset size of 28,413 genomes.

An SSU rRNA phylogenetic tree was used to illustrate and map the presence of nitric oxide reductase genes in bacterial genomes. To build this, 16S sequences were aligned with MAFFT v7.471 (Katoh and Standley, 2013) using as a guide tree the topology of the NCBI taxonomy in

which nodes with fewer than or equal to 2000 terminal descendants were transformed in polytomies. Sequences descending from each node were aligned separately and the alignments were then merged. Using the complete 16S alignment, the % identity was estimated amongst the 403,635,078 possible pairs of genomes.

A maximum-likelihood tree was built using IQTREE v2.1.2 (Nguyen *et al.*, 2015), with the guide tree as a constraint. The topology obtained contains all major relevant bacterial groups, however deep-branching relationships do not reflect evolutionary histories; the tree was rooted arbitrarily using the *Deferribacteres* as an outgroup.

Genomes were screened using BLAST searches (version 2.11.0; Camacho *et al.*, 2009) to assess whether each contained nitric oxide reductase and photosynthesis genes. Phylogenetic gene trees for each gene were built to assess orthology.

For photosynthesis (Cardona, 2015) these genes were used as markers: *psaB* (photosystem I, *pshA* (type I reaction centres,), *psbA* (photosystem II,), *pufL* (type II reaction centres,). For NO reductase, these genes were screened: *norV* (Shimizu *et al.*, 2015), *norB* (i.e. the *cnorB* gene, which encodes for a protein that reduces NO using cytochromes as electron donors, and the *qnorB* gene, which encodes for a protein that uses electrons from quinol (Braker and Tiedje, 2003)), and *hmpA* (encoding a flavohemoglobin implicated in NO detoxification; (Hernández-Urzúa *et al.*, 2003; Forrester and Foster, 2012). Query sequences for all genes above and their accession number are found in Supplementary File S1.

To obtain a better readability of the tree, the branches in Figure 5 and Figure S9 were collapsed based on a 16S % identity threshold. In Figure 5 we used a threshold of 97%, while in Figure S9 we used a threshold of 90%. Additionally, in Figure 5 all non-photosynthetic strains

559 were pruned from the tree. In all figures, the tips representing the four strains that were cultured in
560 this study were always kept as individual tips, regardless of their identity score.
561

562 **FIGURES**

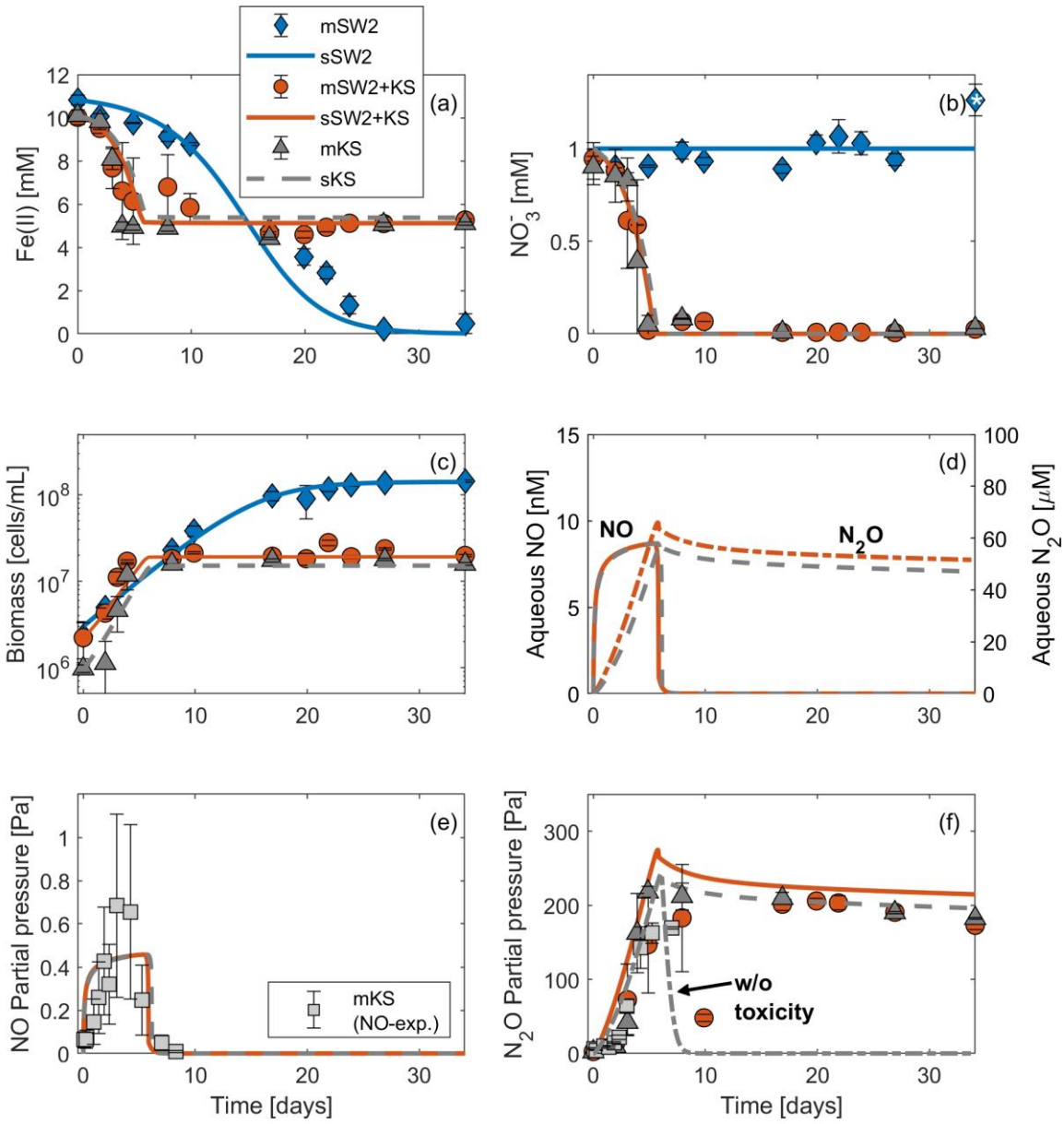

563
564 **Figure 1.** Aqueous and gas phase time-series measured (m) and simulated (s) concentrations for
565 phototrophic Fe(II) oxidation by *R. ferrooxidans* SW2, nitrate dependent Fe(II) oxidation by KS,
566 and a mixed KS plus *R. ferrooxidans* SW2 incubation. (a) Fe(II) oxidation. (b) NO_3^- reduction. (c)
567 Total cell numbers measured by flow cytometry. (d) Predicted aqueous concentrations of NO and
568 N_2O. (e) Predicted NO partial pressure compared to measured NO values in culture KS performed
569 during a parallel incubation (square markers). (f) Predicted and measured N_2O partial pressures.
570 Also included is the model prediction for N_2O when no NO toxicity term is included which
571 validates the assertion that some inhibition of the KS culture occurs later in the growth phase which
572 inhibits further N_2O reduction. Gaseous reactive intermediates nitric and nitrous oxide were only

573 present in the KS and mixed KS plus *R. ferrooxidans* SW2 incubations. Star in figure 1b indicates
574 potential outlier in data.
575

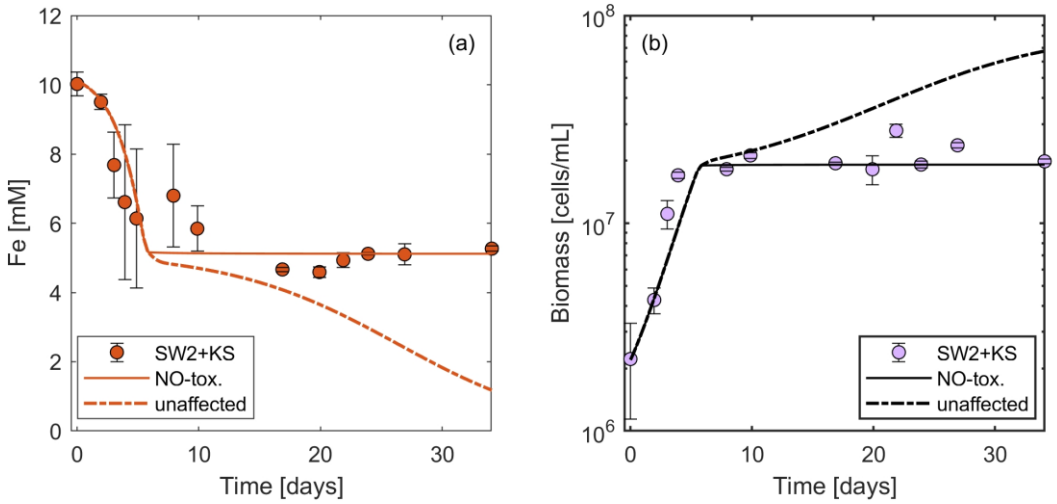

Figure 2. Comparison of measured values for Fe(II) oxidation (a) and cell growth (b) in the mixed culture and in the numerical model where both with (NO-tox) and without (unaffected) NO toxicity included. Measured values for Fe(II) oxidation and cell growth are lower than would be predicted if there was no interaction between the nitrate-reducing Fe(II)-oxidizer and photoferrotroph. The model successfully captures the observed data when sensitivity of the photoferrotroph to NO is included.

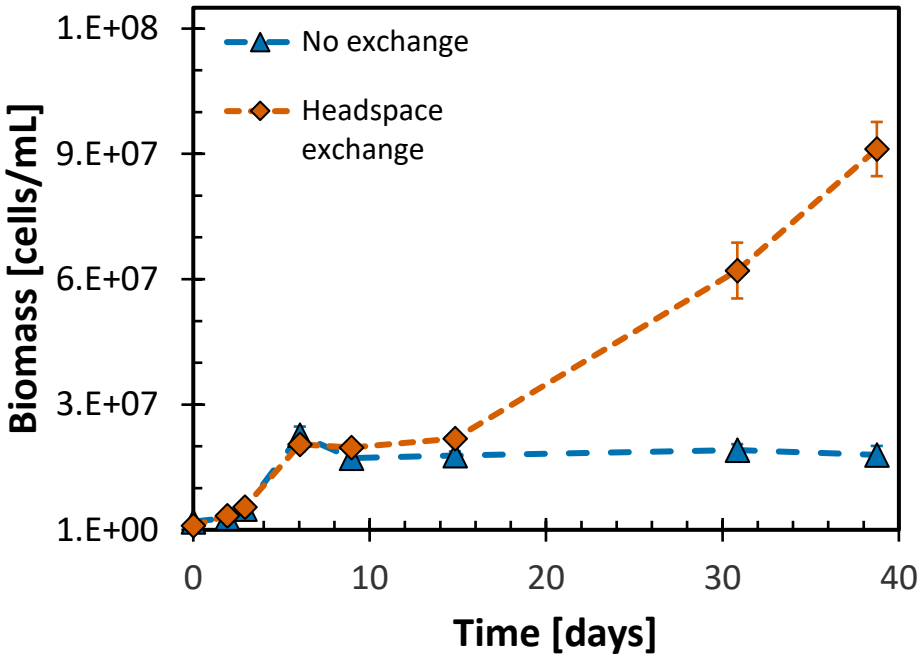

585

586 **Figure 3.** Cell numbers measured by flow cytometry in incubations containing both KS and *R.*
587 *ferrooxidans* SW2. Orange is headspace exchanged with N_2/CO_2 gas mix after sampling, while
588 blue is no headspace exchange. Exchange of the headspace after each sampling point in a KS- *R.*
589 *ferrooxidans* SW2 mixed incubation results in alleviation of the inhibition of phototrophic Fe(II)
590 oxidizers. Errors are standard deviations of biological triplicates.
591

592

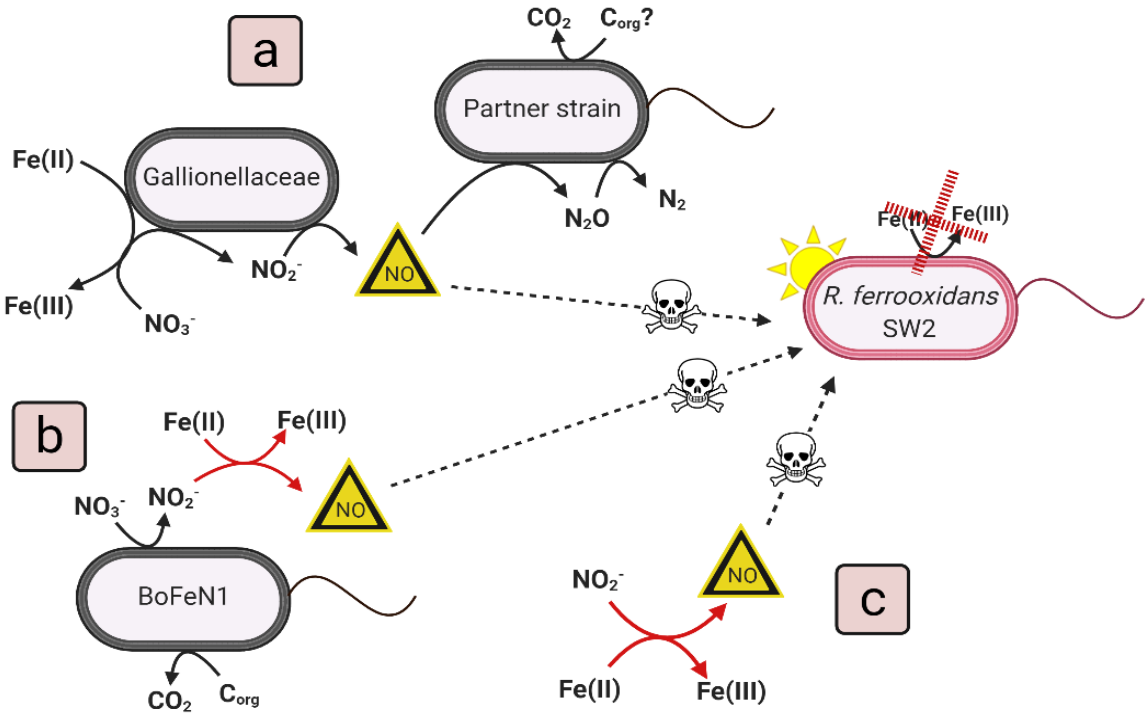

593

594 Figure 4. Schematic of NO production and phototroph inhibition by NO via 3 mechanisms of
595 nitrate-reducing Fe(II) oxidation. (A) The Fe(II)-oxidizer of culture KS (*Gallionella*) produces NO
596 via denitrification coupled to enzymatic Fe(II) oxidation. Some NO may be scavenged by
597 heterotrophic partner strains (dominated by *Bradyrhizobium*) or may interact with the phototroph
598 causing inhibition. It is also possible that some nitrite reacts with Fe(II) abiotically in this scenario.
599 Nb. Our model does not simulate the individual contribution of the components of the KS culture
600 but models the culture as a whole. (B) The non-enzymatic Fe(II)-oxidizer *Acidovorax* sp. BoFeN1
601 produces nitrite during heterotrophic denitrification, which oxidizes Fe(II) abiotically and produces
602 NO. (C) Nitrite reacts abiotically with Fe(II) and produces NO. In all cases NO inhibits
603 photoferrotroph activity.
604

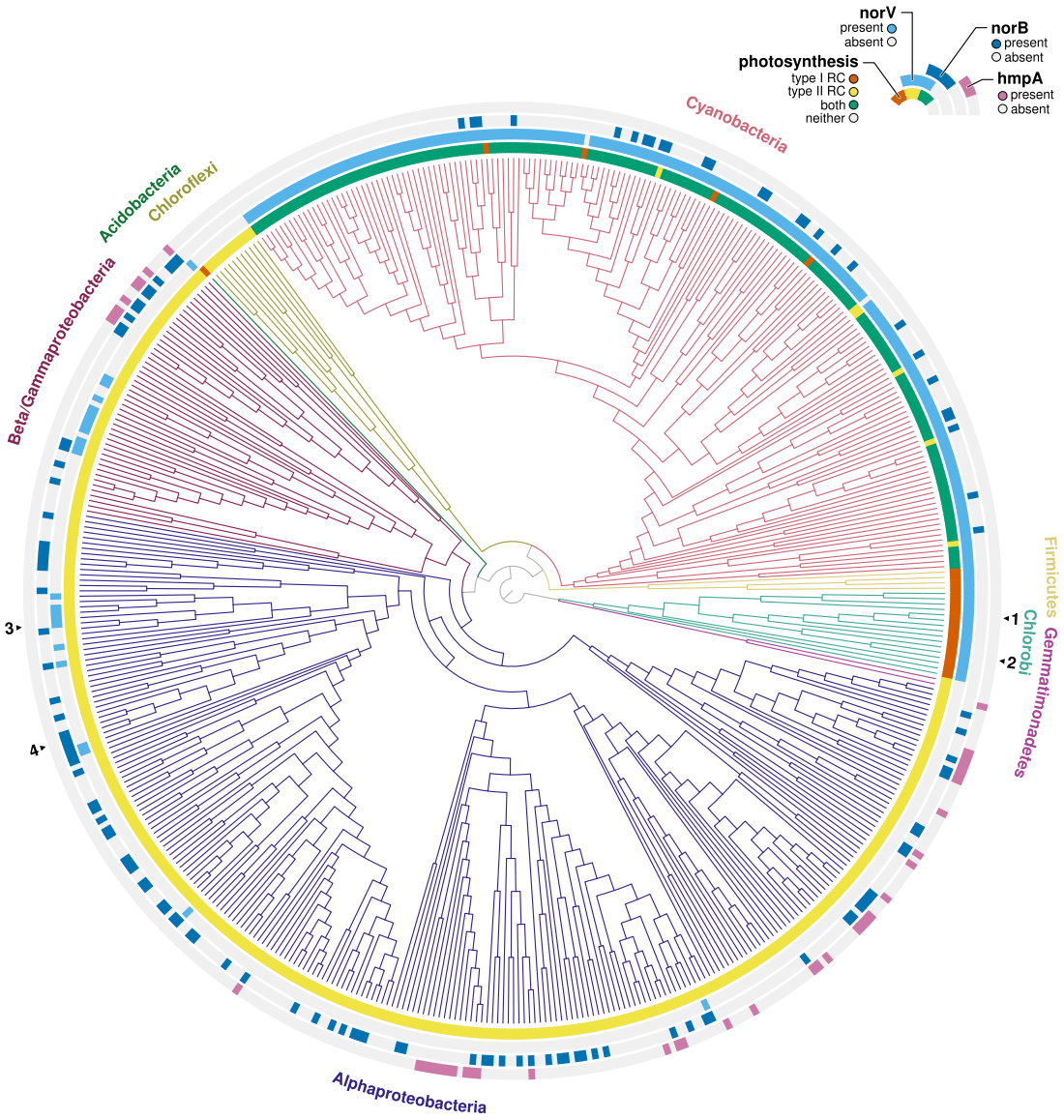

Figure 5. Distribution of nitric oxide reduction genes in genomes of phototrophic bacteria. Anoxygenic phototrophs were identified by possession of genes encoding for Type I (pshA) or Type II (pufL) reaction centers. Cyanobacteria are identified by the presence of genes for both types of reaction center, photosystem I (psaB) and photosystem II (psbA). The presence of norV, norB and hmpA are indicated by light blue, dark blue, or pink annotations, respectively. NorV is ubiquitous in the Chlorobi and Cyanobacteria but is less common in anoxygenic phototrophs with Type II reaction centers. Numbers denote positions of the 4 photoferrotrophs cultured in this study: (1) *Chlorobium ferrooxidans* KoFox, (2) *Chlorobium* sp. N1, (3) *Rhodovulum robiginosum*, and (4) *Rhodobacter ferrooxidans* SW2. Branches were collapsed based on a 16S % identity threshold of 97%. Tips representing the four strains cultured in this study were kept as individual tips, regardless of their identity score.

References

Almeida, J.., Julio, S.., Reis, M.A.., and Carrondo, M.J.. (1995) Nitrite inhibition of denitrification by Pseudomonas fluorescens. *Biotechnol Bioeng* **46**: 194–201.

Altabet, M.A. and Francois, R. (1994) Sedimentary nitrogen isotopic ratio as a recorder for surface ocean nitrate utilization. *Global Biogeochem Cycles* **8**: 103–116.

Belli, K.M., DiChristina, T.J., Van Cappellen, P., and Taillefert, M. (2015) Effects of aqueous uranyl speciation on the kinetics of microbial uranium reduction. *Geochim Cosmochim Acta* **157**: 109–124.

Blank, C.. and Sánchez-Baracaldo, P. (2010) Timing of morphological and ecological innovations in the cyanobacteria–a key to understanding the rise in atmospheric oxygen. *Geobiology* **8**: 1–23.

Blöthe, M. and Roden, E.E. (2009) Composition and activity of an autotrophic Fe(II)-oxidizing, nitrate-reducing enrichment culture. *Appl Environ Microbiol* **75**: 6937–6940.

Braker, G. and Tiedje, J.M. (2003) Nitric oxide reductase (norB) genes from pure cultures and environmental samples. *Appl Environ Microbiol* **69**: 3476–3483.

Bryce, C., Blackwell, N., Schmidt, C., Otte, J., Huang, Y., Kleindienst, S., et al. (2018) Microbial anaerobic Fe(II) oxidation – ecology, mechanisms and environmental implications. *Environ Microbiol* **20**: 3462–3483.

Busigny, V., Lebeau, O., Ader, M., Krape, B., and Bekker, A. (2013) Nitrogen cycle in the Late Archean ferruginous ocean. *Chem Geol* **362**: 115–130.

Camacho, C., Coulouris, G., Avagyan, V., Ma, N., Papadopoulos, J., Bealer, K., and Madden, T.L. (2009) BLAST+: Architecture and applications. *BMC Bioinformatics* **10**: 1–9.

Canfield, D.E., Glazer, A.N., and Falkowski, P.G. (2010) The evolution and future of earth's nitrogen cycle. *Science* **330**: 192–196.

Cardona, T. (2015) A fresh look at the evolution and diversification of photochemical reaction centers. *Photosynth Res* **126**: 111–134.

Chen, J. and Strous, M. (2013) Denitrification and aerobic respiration, hybrid electron transport chains and co-evolution. *Biochim Biophys Acta* **1827**: 136–144.

Czaja, A.D., Johnson, C.M., Beard, B.L., Roden, E.E., Li, W., and Moorbath, S. (2013) Biological Fe oxidation controlled deposition of banded iron formation in the ca . 3770 Ma Isua Supracrustal Belt (West Greenland). *Earth Planet Sci Lett* **363**: 192–203.

Derry, L. (2015) Causes and consequences of mid-Proterozoic anoxia. *Geophys Res Lett* **42**: 8538–8546.

Drummond, J.. and Matthews, R.. (1994) Nitrous oxide inactivation of cobalamin-dependent methionine synthase from Escherichia coli: characterization of the damage to the enzyme and prosthetic group. *Biochemistry* **33**: 3742–3750.

Ducluzeau, A.L., van Lis, R., Duval, S., Schoepp-Cothenet, B., Russell, M.J., and Nitschke, W. (2009) Was nitric oxide the first deep electron sink? *Trends Biochem Sci* **34**: 9–15.

Ehrenreich, A. and Widdel, F. (1994) Anaerobic oxidation of ferrous iron by purple bacteria, a new type of phototrophic metabolism. *Appl Environ Microbiol* **60**: 4517–4526.

Eickhoff, M., Obst, M., Schröder, C., Hitchcock, A.P., Tyliszczak, T., Martinez, R.E., et al. (2014) Nickel partitioning in biogenic and abiogenic ferrihydrite: The influence of silica and implications for ancient environments. *Geochim Cosmochim Acta* **140**: 65–79.

Forester, D. and Koon, N. (1969) Mössbauer investigation of metamagnetic FeCO3. *J Appl Phys*

662 **40**: 1316–1317.

663 Forrester, M.T. and Foster, M.W. (2012) Protection from nitrosative stress: A central role for
664 microbial flavohemoglobin. *Free Radic Biol Med* **52**: 1620–1633.

665 Gardner, A.M., Helmick, R.A., and Gardner, P.R. (2002) Flavorubredoxin, an inducible catalyst
666 for nitric oxide reduction and detoxification in Escherichia coli. *J Biol Chem* **277**: 8172–
667 8177.

668 Garvin, J., Buick, R., Anbar, A.D., Arnold, G.L., and Kaufman, A.J. (2009) Isotopic evidence for
669 an aerobic nitrogen cycle in the latest Archean. *Science* **323**: 1045–1048.

670 Godfrey, L. V. and Falkowski, P.G. (2009) The cycling and redox state of nitrogen in the
671 Archaean ocean. *Nat Geosci* **2**: 725–729.

672 Gonser, U. and Grant, P. (1967) Determination of Spin Directions and Electric Field Gradient
673 Axes in Vivianite by Polarized Recoil-Free γ-Rays. *Phys status solidi* **21**: 331–342.

674 Harman, C.E., Felton, R., Hu, R., Domagal-Goldman, S.D., Segura, A., Tian, F., and Kasting,
675 J.F. (2018) Abiotic O 2 Levels on Planets around F, G, K, and M Stars: Effects of
676 Lightning-produced Catalysts in Eliminating Oxygen False Positives . *Astrophys J* **866**: 56.

677 Hartman, H. (1984) The evolution of photosynthesis and microbial mats: A speculation on
678 banded iron formations. In *Microbial mats: stromatolites*. New York: Alan R. Liss, Inc., pp.
679 449–453.

680 He, S., Tominski, C., Kappler, A., Behrens, S., and Roden, E.E. (2016) Metagenomic analyses of
681 the autotrophic Fe(II)-oxidizing, nitrate-reducing enrichment culture KS. *Appl Environ*
682 *Microbiol* **82**: 2656–2668.

683 Hernández-Urzúa, E., Mills, C.E., White, G.P., Contreras-Zentella, M.L., Escamilla, E.,

Vasudevan, S.G., et al. (2003) Flavohemoglobin Hmp, but not its individual domains, confers protection from respiratory inhibition by nitric oxide in Escherichia coli. *J Biol Chem* **278**: 34975–34982.

Homyak, P.M., Kamiyama, M., Sickman, J.O., and Schimel, J.P. (2016) Acidity and organic matter promote abiotic nitric oxide production in drying soils. *Glob Chang Biol* **23**: 1735–1747.

Hu, Z., Wessels, H.J.C.T., van Alen, T., Jetten, M.S.M., and Kartal, B. (2019) Nitric oxide-dependent anaerobic ammonium oxidation. *Nat Commun* **10**:.

Jamieson, J., Prommer, H., Kaksonen, A., Siade, A., Yusov, A., and Bostick, B.C. (2018) Identifying and quantifying the intermediate processes during nitrate dependent iron (II) oxidation. *Environ Sci Technol*.

Jones, C., Nomosatryo, S., Crowe, S.A., Bjerrum, C.J., and Canfield, D.E. (2015) Iron oxides, divalent cations, silica, and the early earth phosphorus crisis. *Geology* **43**: 135–138.

Kampschreur, M.J., Kleerebezem, R., de Vet, W.W.J.M., and Van Loosdrecht, M.C.M. (2011) Reduced iron induced nitric oxide and nitrous oxide emission. *Water Res* **45**: 5945–5952.

Kappler, A., Pasquero, C., Konhauser, K.O., and Newman, D.K. (2005) Deposition of banded iron formations by anoxygenic phototrophic Fe(II)-oxidizing bacteria. *Geology* **33**: 865–868.

Kasting, J.F. (1990) Bolide impacts and the oxidation state of carbon in the Earth's early atmosphere. *Orig Life Evol Biosph* **20**: 199–231.

Katoh, K. and Standley, D.M. (2013) MAFFT multiple sequence alignment software version 7: Improvements in performance and usability. *Mol Biol Evol* **30**: 772–780.

Klueglein, N. and Kappler, A. (2013) Abiotic oxidation of Fe(II) by reactive nitrogen species in

706 cultures of the nitrate-reducing Fe(II) oxidizer Acidovorax sp . BoFeN1 – questioning the
707 existence of enzymatic Fe(II) oxidation. *Geobiology* **11**: 180–190.

708 Klueglein, N., Zeitvogel, F., Stierhof, Y.-D., Floetenmeyer, M., Konhauser, K.O., and Kappler,
709 A. (2014) Potential role of nitrite for abiotic Fe(II) oxidation and cell encrustation during
710 nitrate reduction by denitrifying bacteria. *Appl Environ Microbiol* **80**: 1051–1061.

711 Konhauser, K.O., Hamade, T., Raiswell, R., Morris, R.C., Ferris, F.G., Southam, G., and
712 Canfield, D.E. (2002) Could bacteria have formed the Precambrian banded iron formations?
713 *Geology* **30**: 1079–1082.

714 Konhauser, K.O., Robbins, L.J., Alessi, D.S., Flynn, S.L., Gingras, M.K., Martinez, R.E., et al.
715 (2018) Phytoplankton contributions to the trace-element composition of Precambrian banded
716 iron formations. *Bull Geol Soc Am* **130**: 941–951.

717 Kuypers, M.M.M., Marchant, H.K., and Kartal, B. (2018) The microbial nitrogen-cycling
718 network. *Nat Rev Microbiol*.

719 Lagesen, K., Hallin, P., Rødland, E.A., Stærfeldt, H.H., Rognes, T., and Ussery, D.W. (2007)
720 RNAmmer: Consistent and rapid annotation of ribosomal RNA genes. *Nucleic Acids Res* **35**:
721 3100–3108.

722 Laufer, K., Nordhoff, M., R??y, H., Schmidt, C., Behrens, S., Jorgensen, B.B., and Kappler, A.
723 (2016) Coexistence of microaerophilic, nitrate-reducing, and phototrophic Fe(II) oxidizers
724 and Fe(III) reducers in coastal marine sediment. *Appl Environ Microbiol*.

725 Mancinelli, R.. and McKay, C. (1988) The evolution of nitrogen cycling. *Orig Life Evol Biosph*
726 **18**: 311–325.

727 Mather, T.A., Pyle, D.M., and Allen, A.G. (2004) Volcanic source for fixed nitrogen in the early

Earth's atmosphere. *Geology* **32**: 905–908.

Melton, E.D., Schmidt, C., and Kappler, A. (2012) Microbial iron(II) oxidation in littoral freshwater lake sediment: The potential for competition between phototrophic vs. nitrate-reducing iron(II)-oxidizers. *Front Microbiol* **3**: 1–12.

Melton, E.D., Stief, P., Behrens, S., Kappler, A., and Schmidt, C. (2014) High spatial resolution of distribution and interconnections between Fe- and N-redox processes in profundal lake sediments. **16**: 3287–3303.

Mettam, C., Zerkle, A.L., Claire, M.W., Prave, A.R., Poulton, S.W., and Junium, C.K. (2019) Anaerobic nitrogen cycling on a Neoarchaean ocean margin. *Earth Planet Sci Lett* **527**: 115800.

Michiels, C.C., Darchambeau, F., Roland, F.A.E., Morana, C., Llirós, M., García-Armisen, T., et al. (2017) Iron-dependent nitrogen cycling in a ferruginous lake and the nutrient status of Proterozoic oceans. *Nat Geosci* **10**: 217–221.

Morris, R.C. (1993) Genetic modelling for banded iron-formation of the Hamersley Group, Pilbara Craton, Western Australia. *Precambrian Res* **60**: 243–286.

Nguyen, L.T., Schmidt, H.A., Von Haeseler, A., and Minh, B.Q. (2015) IQ-TREE: A fast and effective stochastic algorithm for estimating maximum-likelihood phylogenies. *Mol Biol Evol* **32**: 268–274.

Ni, B., Ruscalleda, M., Pellicer-Nacher, C., and Smets, B.. (2011) Modeling nitrous oxide production during biological nitrogen removal via nitrification and denitrification: extensions to the general ASM models. *Environ Sci Technol* **45**: 7768.

O'Leary, N.A., Wright, M.W., Brister, J.R., Ciufo, S., Haddad, D., McVeigh, R., et al. (2016)

Reference sequence (RefSeq) database at NCBI: Current status, taxonomic expansion, and functional annotation. *Nucleic Acids Res* **44**: D733–D745.

Otte, J.., Harter, J., Laufer, K., Blackwell, N., Kappler, A., and Kleindienst, S. (2018) The distribution of active iron cycling bacteria in marine and freshwater sediments is decoupled from geochemical gradients. *Environ Microbiol* **20**: 2483–2499.

Pecoits, E., Smith, M.L., Catling, D.C., Philippot, P., Kappler, A., and Konhauser, K.O. (2015) Atmospheric hydrogen peroxide and Eoarchean iron formations. *Geobiology* **13**: 1–14.

Rancourt, D.G. and Ping, J.Y. (1991) Voigt-based methods for arbitrary-shape static hyperfine parameter distributions in Mössbauer spectroscopy. *Nucl Inst Methods Phys Res B* **58**: 85–97.

Ranjan, S., Todd, Z.R., Rimmer, P.B., Sasselov, D.D., and Babbin, A.R. (2019) Nitrogen Oxide Concentrations in Natural Waters on Early Earth. *Geochemistry, Geophys Geosystems* **20**: 2021–2039.

Sánchez-Baracaldo, P. (2015) Origin of marine planktonic cyanobacteria. *Sci Rep* **5**:.

Santana, M.M., Gonzalez, J.M., and Cruz, C. (2017) Nitric Oxide Accumulation : The Evolutionary Trigger for Phytopathogenesis. *Front Microbiol* **8**: 1–13.

Saraiva, L.M., Vicente, J.B., and Teixeira, M. (2004) The role of the flavodiiron proteins in microbial nitric oxide detoxification. In *Advances in Micobial Physiology*. Poole, R. (ed)., pp. 78–120.

Saraste, M. and Castresana, J. (1994) Cytochrome oxidase evolved by tinkering with denitrification enzymes. *FEBS Lett* **341**: 1–4.

Schoch, C.L., Ciufo, S., Domrachev, M., Hotton, C.L., Kannan, S., Khovanskaya, R., et al.

(2020) NCBI Taxonomy: A comprehensive update on curation, resources and tools. *Database* **2**: 1–21.

Schreiber, F., Loeffler, B., Polerecky, L., Kuypers, M.., and De Beer, D. (2009) Mechanisms of transient nitric oxide and nitrous oxide production in a complex biofilm. *ISME J* **3**: 1301–1313.

Schreiber, F., Polerecky, L., and de Beer, D. (2008) Nitric oxide microsensor for high spatial resolution measurements in biofilms and sediments. *Anal Chem* **80**: 1152–1158.

Schreiber, F., Stief, P., Kuypers, M.M.M., and de Beer, D. (2014) Nitric oxide turnover in permeable river sediment. *Limnol Oceanogr* **59**: 1310–1320.

Shimizu, T., Hirai, S., Yokoyama, E., Ichimura, K., and Noda, M. (2015) An evolutionary analysis of nitric oxide reductase gene norV in enterohemorrhagic Escherichia coli O157. *Infect Genet Evol* **33**: 176–181.

Stanton, C.L., Reinhard, C.T., Kasting, J.F., Ostrom, N.E., Haslun, J.A., Lyons, T.W., and Glass, J.B. (2018) Nitrous oxide from chemodenitrification: A possible missing link in the Proterozoic greenhouse and the evolution of aerobic respiration. *Geobiology* **16**: 597–609.

Straub, K.L., Benz, M., Schink, B., and Widdel, F. (1996) Anaerobic, nitrate-dependent microbial oxidation of ferrous iron. *Appl Environ Microbiol* **62**: 1458–60.

Stüeken, E.E., Kipp, M.A., Koehler, M.C., and Buick, R. (2016) The evolution of Earth's biogeochemical nitrogen cycle. *Earth Sci Rev* **160**: 220–239.

Summers, D.P. and Khare, B. (2007) Nitrogen Fixation on Early Mars and Other Terrestrial Planets: Experimental Demonstration of Abiotic Fixation Reactions to Nitrite and Nitrate. *Astrobiology* **7**: 333–341.

794 Thompson, K.J., Kenward, P.A., Bauer, K.W., Warchola, T., Gauger, T., Martinez, R., et al.
795 (2019) Photoferrotrophy, deposition of banded iron formations, and methane production in
796 Archean oceans. *Sci Adv* **5**: 1–9.

797 Tominski, C., Heyer, H., Lösekann-Behrens, T., Behrens, S., and Kappler, A. (2018) Growth and
798 population dynamics of the anaerobic Fe(II)-oxidizing and nitrate-reducing enrichment
799 culture KS. *Appl Environ Microbiol* **84**: 1–15.

800 Wang, Y., Desilva, A.W., Goldenbaum, G.C., and Dickerson, R.R. (1998) Nitric oxide
801 production simulated by lightning: Dependence on current, energy and pressure. *J Geophys*
802 *Res* **103**: 19148–19159.

803 Widdel, F. and Bak, F. (1992) The Prokaryotes: A Handbook on the Biology of Bacteria:
804 Ecophysiology, Isolation, Identification, and Applications., New York: Springer-Verlag,
805 New York.

806 Widdel, F. and Pfenning, N. (1981) Studies on Dissimilatory Sulfate-Reducing Bacteria that
807 Decompose Fatty Acids. *Arch Microbiol* **129**: 395–400.

808 Widdel, F., Schnell, S., Heising, S., Ehrenreich, A., Assmus, B., and Schink, B. (1993) Ferrous
809 iron oxidation by anoxygenic phototrophic bacteria. *Nature* **362**: 834–836.

810 Wong, M.L., Charnay, B.D., Gao, P., Yung, Y.L., and Russell, M.J. (2017) Nitrogen Oxides in
811 Early Earth's Atmosphere as Electron Acceptors for Life's Emergence. *Astrobiology* **17**:
812 975–983.

813 Zerkle, A.L., House, C.H., Cox, R.P., and Canfield, D.E. (2006) Metal limitation of
814 cyanobacterial N2 fixation and implications for the Precambrian nitrogen cycle. *Geobiology*
815 **4**: 285–297.

816 Zerkle, A.L., Poulton, S.W., Newton, R.J., Mettam, C., Claire, M.W., Bekker, A., and Junium,
817 C.K. (2017) Onset of the aerobic nitrogen cycle during the Great Oxidation Event. *Nature*
818 1–10.

819

Acknowledgments: We would like to thank Ellen Roehm for assistance in the cultivation experiments, particularly with the nitrate measurements, and Daniel Buchner for assistance with measurement of N_2O. We also thank James Byrne for assistance with the interpretation of the Moessbauer data.

Funding: C.B and V.N are grateful for support from Deutsche Forschungsgemeinschaft Individual Research Grant BR-5927/2-1. GB was supported by a University of Bristol Scholarship. Funding support for the bioinformatics aspects of this work came from a Royal Society University Research Fellowship to P.S.-B. S.B. was supported by NASA's Nexus for Exoplanet System Science (NExSS) research coordination network at Arizona State University. A.K. acknowledges the infrastructural support by the DFG under Germany's Excellence Strategy, cluster of Excellence EXC2124, project ID 390838134

Author contributions: C.B and A.K devised the original concept of the study. C.B and V.N designed the study, conducted the laboratory cultivation experiments, analysed and interpreted the data, and wrote the manuscript. A.M was responsible for all mathematical modelling. G.B and P.S.B conducted the genomic surveys. S.B, L.S and S.G ran additional laboratory incubations. M.S was responsible for Moessbauer spectroscopy. K.K and A.L.Z assisted in the interpretation of the data and its wider implications. All authors contributed to the interpretation of results and preparation of the manuscript.

Competing interests: Authors declare no competing interests.

Data and materials availability: Supplementary data associated with the bioinformatics and model sensitivity analysis are included in the supplementary information. Model outputs and scripts are available to the reviewers upon request. On acceptance of the final manuscript version, all raw data and scripts will be uploaded to the open access data repository "Zenodo".

Supplementary Materials:

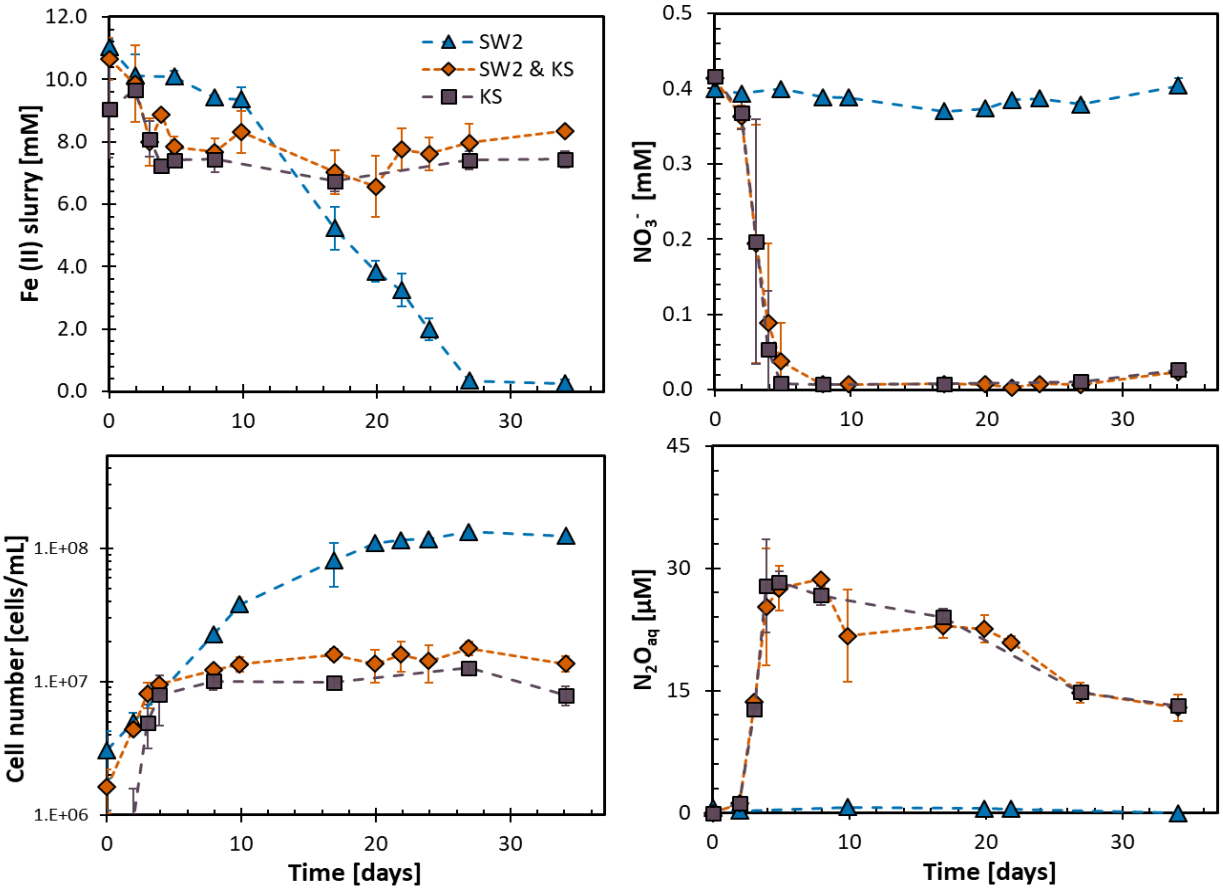

Supplementary Figure S1. Competition dynamics between phototrophic and nitrate-dependent Fe(II)-oxidizers (*Rhodobacter ferroxidans* strain SW2 and enrichment culture KS) with limited nitrate (0.4 mM), showing that the mixed culture behaves similarly to the nitrate-reducing culture with regards to all parameters, and Fe(II) oxidation in the mixed culture is incomplete.

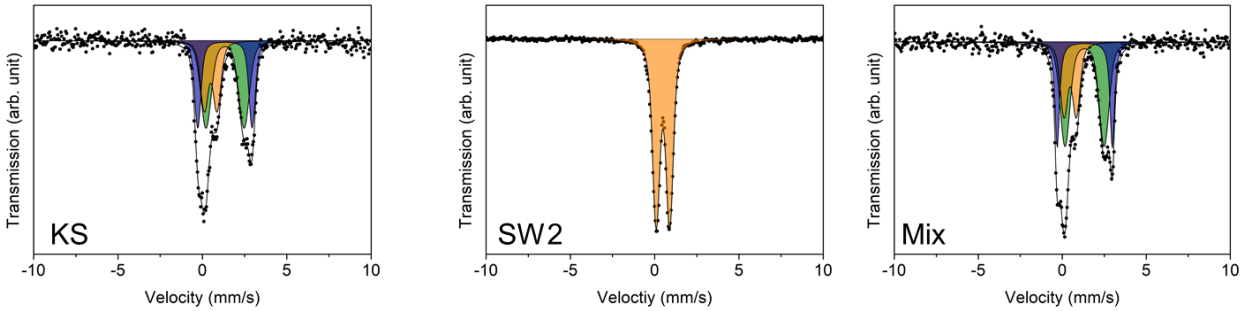

Supplementary Figure S2: Moessbauer spectra of minerals formed by KS (left), ***R. ferrooxidans*** **SW2 (middle) and the mixed incubation of both strains (right).** Closed circles represent collected data, while the solid black line represents the data fit. Orange shaded areas represent a short-range ordered (SRO) Fe(III) mineral; the green shaded area siderite; and the blue shaded area a second Fe(II) mineral phase, possibly vivianite. *R. ferrooxidans* SW2 exclusively formed a SRO Fe(III) mineral, possibly ferrihydrite. Both, the KS and mixed incubations contain Fe(II) as well as Fe(III) mineral phases.

862 **Table S1: Hyperfine parameters of the mineral products of setups KS,** *R. ferrooxidans* **SW2 and Mix**
863 **incubation. Results of the fitting spectra.** δ – center shift, ΔEQ – quadrupole splitting, R.A. – relative
864 abundance of the mineral phase at the given temperature, ± - error in the relative abundance, χ2 indicates
865 the goodness of fit. [1] (Forester and Koon, 1969), [2] (Eickhoff *et al.*, 2014), [3] (Gonser and Grant, 1967).
866

Sample	Temp [K]	Phase	δ [mm s^{-1}]	ΔE_Q [mm s^{-1}]	R. A. [%]	±	χ^2
KS	77	Siderite[1]	1.34	2.26	43.9	8.2	0.62
		Ferrihydrite[2]	0.49	0.76	26.7	4.5	
		Vivianite[3]	1.33	3.22	29.3	8.6	
SW2	77	Ferrihydrite[2]	0.49	0.80	100	-	1.58
Mix	77	Siderite[1]	1.33	2.33	47.1	3.7	0.53
		Ferrihydrite[2]	0.47	0.73	26.1	2.3	
		Vivianite[3]	1.34	3.28	26.8	3.8	

867
868

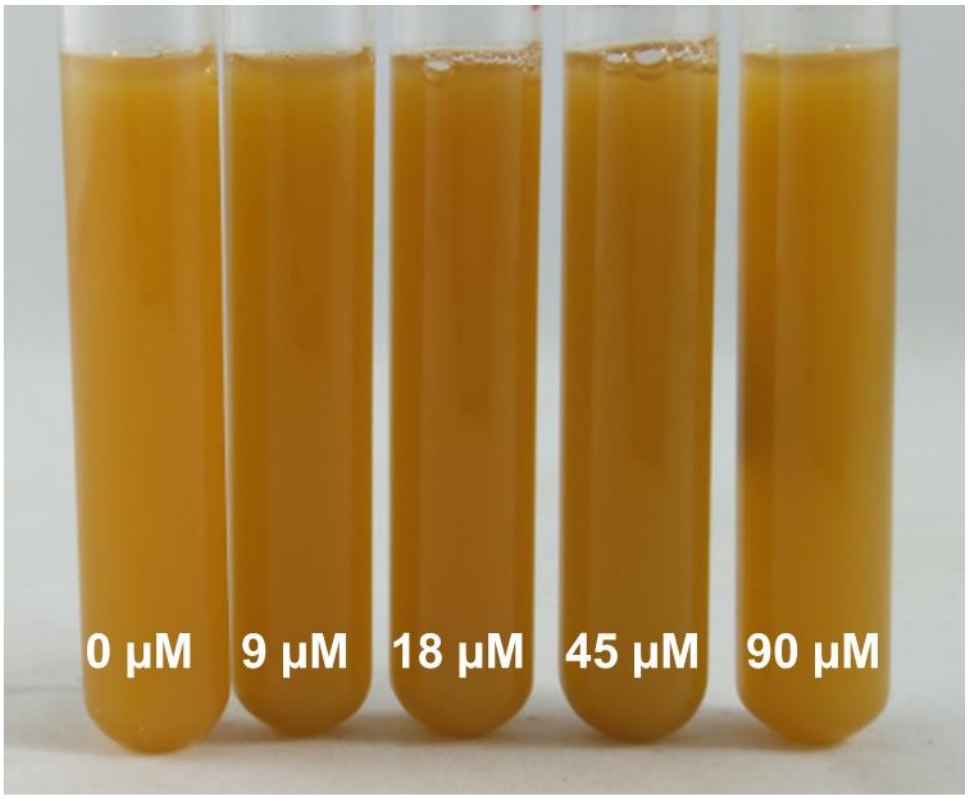

Supplementary Figure S3. Toxicity experiment with $N_2O_{(aq)}$ showing no toxicity and no inhibition of *Rhodobacter ferrooxidans* SW2 with N_2O added at concentrations significantly higher than measured in the experiment.

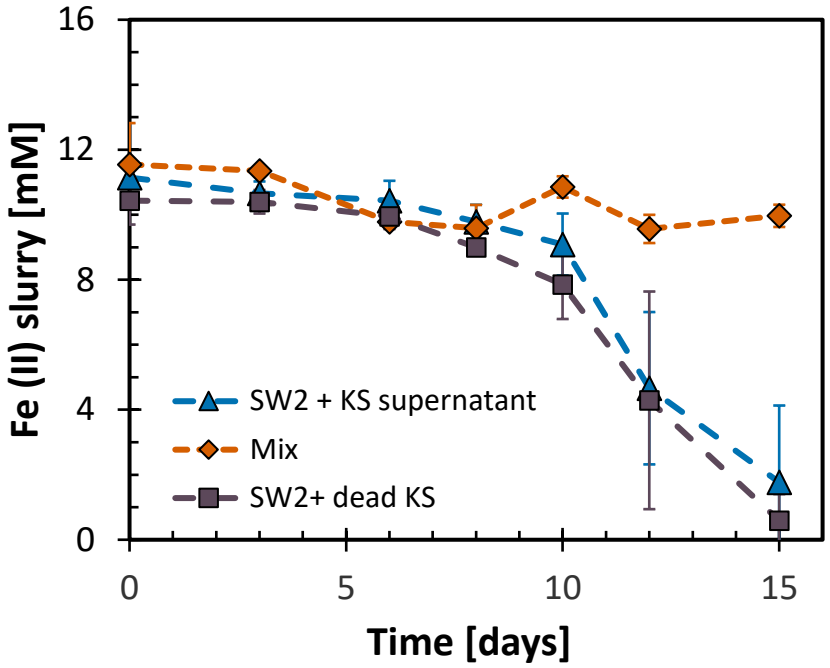

Supplementary Figure S4. Fe(II) oxidation is complete when *R. ferrooxidans* SW2 is combined with dead KS cells (autoclaved prior to inoculation) or with the supernatant from the KS culture (filtered prior to inoculation). Inhibition still occurs when live KS cells are added.

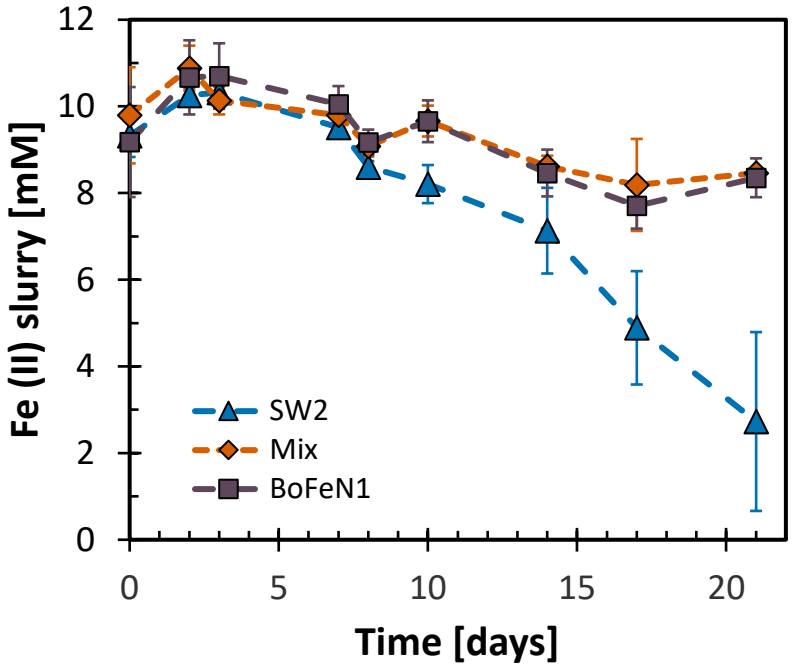

884

885

886 **Supplementary figure S5:** Fe(II) oxidation by *R. ferrooxidans* SW2, *Acidovorax* sp. BoFeN1 and a mixed
887 incubation containing both. Inhibition of SW2 is also observed when this alternative nitrate-reducing Fe(II)-
888 oxidizer is used.

889

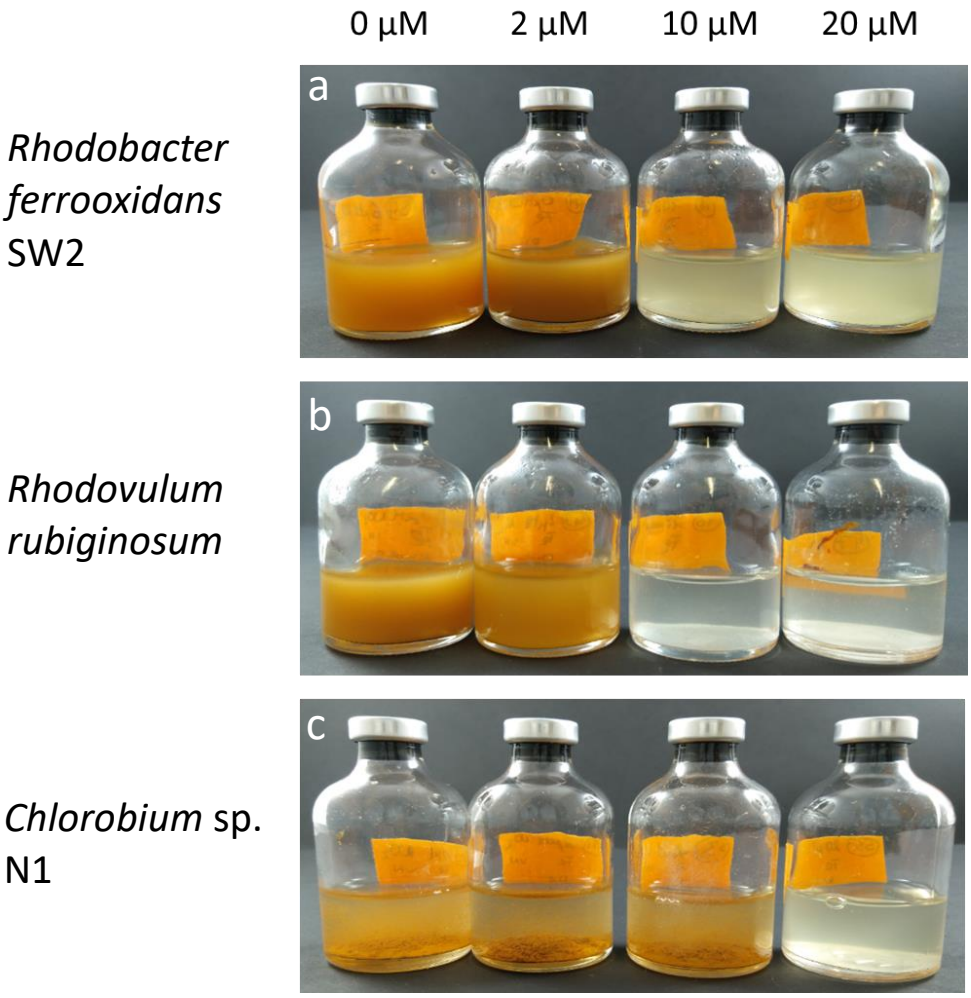

Supplementary figure S6. Photoferrotrophs *R. ferrooxidans* SW2 (top), *Rhodovulum rubiginosum* (middle) and *Chlorobium* sp. N1 (bottom) grown alone with different nitrite concentrations (listed at the top of the figure). All strains show inhibition suggesting the abiotic reaction between nitrite and Fe(II) can be inhibitory if the nitrite concentrations are high enough.

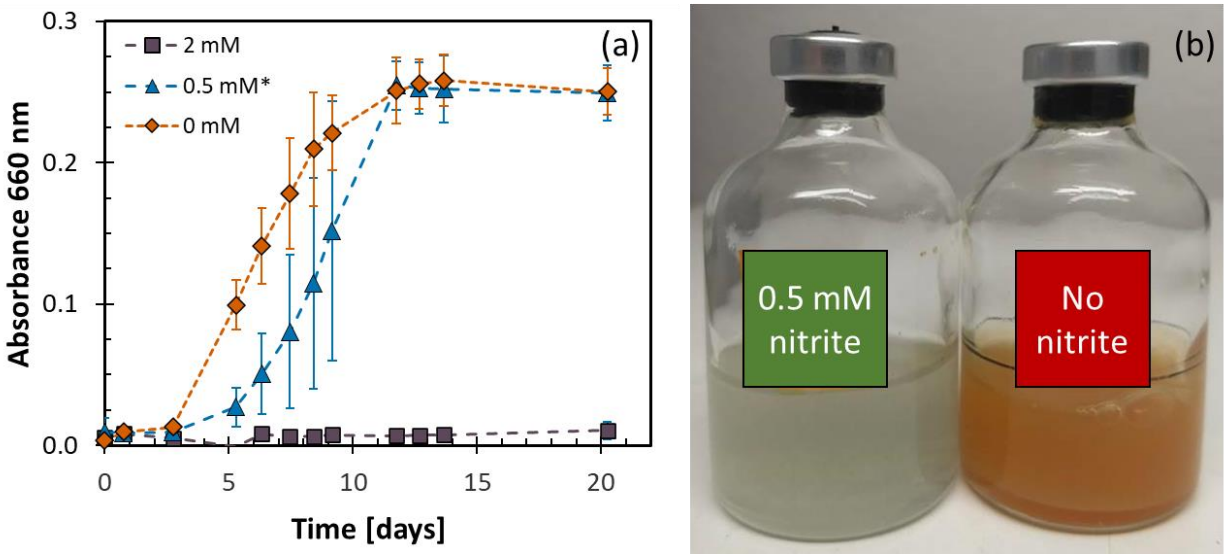

Supplementary Figure S7. A: Growth of *R. ferrooxidans* SW2 cells (measured by absorbance at 660 nm) in the presence of different concentrations of nitrite in the absence of Fe(II). * The 0.5 mM nitrite set up represents duplicate measurements, whilst the others are from biological triplicates. B: Cultures of *R. ferrooxidans* SW2 in the presence and absence of nitrite with 10 mM Fe(II).

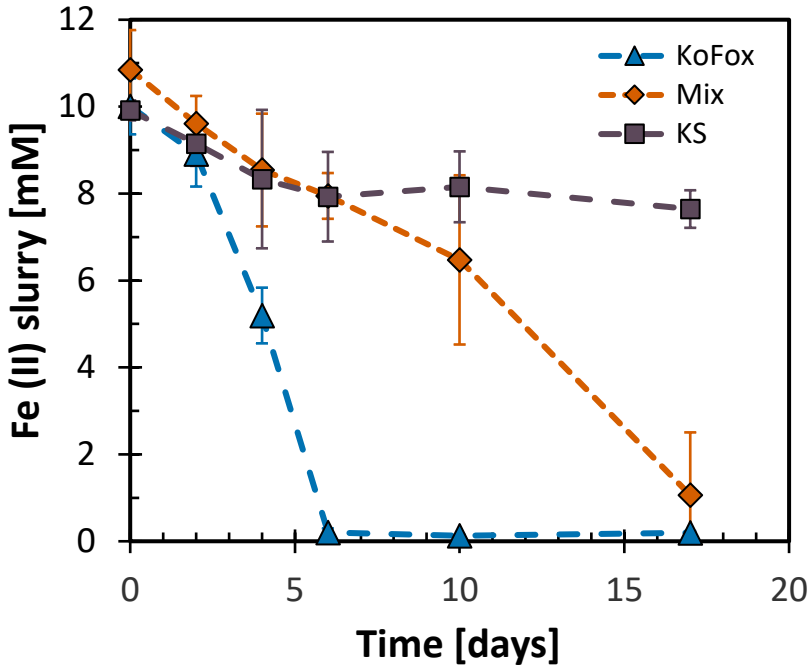

Supplementary Figure S8: Fe(II) oxidation by culture KS, *Chlorobium ferroxidans* sp. KoFox (a freshwater GSB) and an incubation containing both. In this case 0.4 mM nitrate was added. *Chlorobium ferrooxidans* sp. KoFox is also inhibited by KS, but eventually overcomes the inhibition.

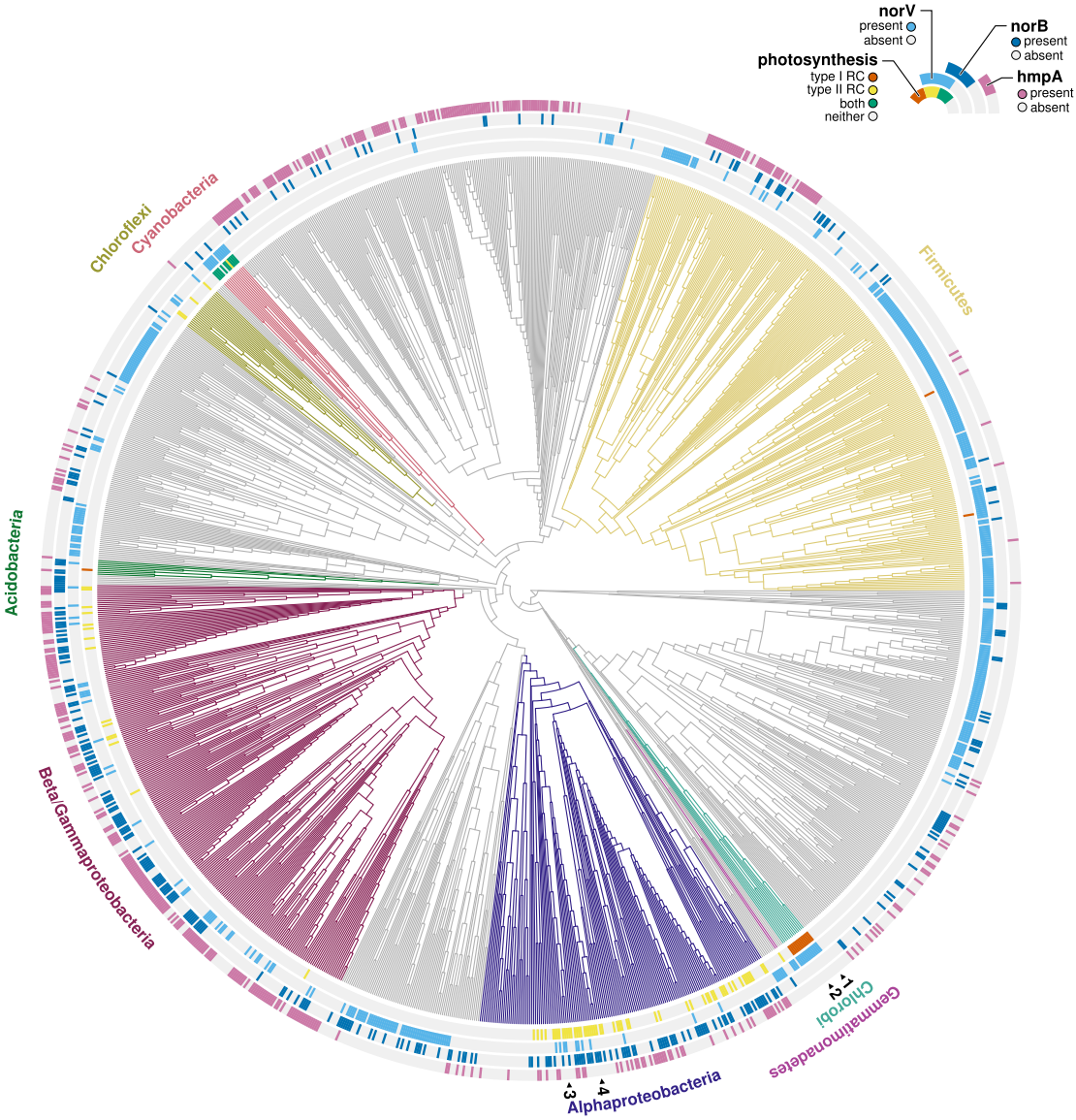

Supplementary figure S9: Distribution of phototrophy and nitric oxide detoxification genes across 14,624 bacterial genomes. Numbers denote positions of the 4 photoferrotrophs cultured in this study: (1) *Chlorobium ferrooxidans* KoFox, (2) *Chlorobium* sp. N1, (3) *Rhodovulum robiginosum*, and (4) *Rhodobacter ferrooxidans* SW2.

916 **Table S2.** Medium composition used for experiments with strains other than *R. ferrooxidans* SW2

917

Strain	Reference	Growth media
Rhdovulum rubiginosum	Straub et al. (1999)	22 mM bicarbonate-buffered media containing following salts: 26.4 g L^{-1} NaCl, 6.8 g L^{-1} $MgSO_4.7H_20$, 5.7 g L^{-1} $MgCl_2.6H_2O$, 1.5 g L^{-1} $CaCl_2.2H_2O$, 0.66 g L^{-1} KCl, 0.09 g L^{-1} KBr 0.4 g L^{-1} KH_2PO_4, 0.25 g L^{-1} NH_4Cl Additives: 1 mL L^{-1} sterile filtered 7-vitamin solution (Widdel and Pfennig, 1981), trace element solution (Widdel et al., 1983) and selenite-tungstate solution (Widdel and Bak, 1992) pH: 7.0 Added substrates: 10 mM $FeCl_2$
Chlorobium sp. N1	Laufer et al. (2016)	22 mM bicarbonate-buffered media containing following salts: 17.3 g L^{-1} NaCl, 0.025 g L^{-1} $MgSO_4.7H_20$, 8.6 g L^{-1} $MgCl_2.6H_2O$, 0.99 g L^{-1} $CaCl_2.2H_2O$, 0.39 g L^{-1} KCl, 0.059 g L^{-1} KBr, 0.05 g L^{-1} KH_2PO_4, 0.25 g L^{-1} NH_4Cl Additives: 1 mL L^{-1} sterile filtered 7-vitamin solution (Widdel and Pfennig, 1981), trace element solution (Widdel et al., 1983) and selenite-tungstate solution (Widdel and Bak, 1992) pH: 7.0 Added substrates: 10 mM $FeCl_2$
Acidovorax sp. BoFeN1		22 mM bicarbonate-buffered media containing following salts: 0.6 g/L KH_2PO_4, 0.3 g/L NH_4Cl, 0.025 g/L $MgSO_4 \cdot 7\ H_2O$, 0.4 g/L $MgCl_2 \cdot 6\ H_2O$, 0.1 g/L $CaCl_2 \cdot 2\ H_2O$ Additives: 1 mL L^{-1} sterile filtered 7-vitamin solution (Widdel and Pfennig, 1981), trace element solution (Widdel et al., 1983) and selenite-tungstate solution (Widdel and Bak, 1992) pH: 7.0 Added substrates: 10 mM $FeCl_2$, 2 mM nitrate, 0.5 mM sodium acetate

Supplementary Method 1: Parameter uncertainty and sensitivity analysis

Relative parameter uncertainties were estimated via a linearized uncertainty analysis on the log-transformed parameters and are reported on the matrix-diagonal in Figure S1, along with the correlation coefficients of log-parameter uncertainties. In addition, results from a linearized sensitivity analysis obtained via the automated model calibration (of the log-parameter values) procedure are presented in Figures S1 and S2 for the SW2 and KS-only incubations. The kinetic parameters for N_2O reduction exhibit high relative uncertainty estimates. The NO threshold concentration, $\boldsymbol{C_{thresh}^{NO}}$, has the highest estimate of relative uncertainty and is poorly constrained in our model. The latter is due, in part, to the sharp concentration behavior simulated during both the increase and decrease of NO in the system. Thus, relatively large changes in the $\boldsymbol{C_{thresh}^{NO}}$ would still yield similar exposure times to NO and a similar toxicity response.

The model output is sensitive to most parameters, in both SW2 and KS variants. Most notably, the parameters with the lowest sensitivities are $\boldsymbol{C_{thresh}^{NO}}$, $\boldsymbol{K_{NO}}$ and $\boldsymbol{K_{Fe}^{KS}}$, corresponding to parameters with higher relative uncertainty estimates. The strong correlation (1:1) between $\boldsymbol{\mu_{max}^{ph}}$ and $\boldsymbol{K_{Fe}^{ph}}$ in the ***R. ferrooxidans*** SW2 incubation suggests that, for this particular experiment, our model can only reliably determine the ratio of both parameters and not their absolute value. Thereby, implying that the Monod-expression is effectively in the first-order range.

The overall root mean squared error (RMSE) for each model was computed by considering the difference between measured and simulated values for all data-types, normalized by each measurement's standard deviation. In addition, we computed RMSE values for each data type to highlight the model accuracy for each measurement. All data-specific RMSE values fall within measurement standard deviation bounds. Without the inclusion of NO-toxicity, the overall RMSE for the KS incubation is nearly double of that with toxicity, 7.88 and 15.29, respectively.

To our knowledge, the only previously published work that simulated NDFO is that of Jamieson et al. (2018). The model formulation presented herein and that in Jamieson et al. (2018) differ, in particular, with regards to the number of denitrification steps considered. However, both sets of calibrated electron

acceptor and donor half saturation coefficients fall within the same order of magnitude. The electron acceptor half-saturation coefficients calibrated in this study fall close to the 3.5×10^{-3} [mM] electron acceptor half-saturation coefficient and 7.59 [mM] "encrustation inhibition coefficient" (equivalent to K_{Fe}^{KS}, herein) presented in Jamieson *et al.*, (2018). Moreover, our fitted electron acceptor half-saturation constants and maximum specific growth rate constants (μ_{max}) fall within the range of previously reported denitrification parameters (e.g., Almeida *et al.*, 1995; Schreiber *et al.*, 2009; Ni *et al.*, 2011), albeit coupled to organic carbon as the electron donor. Notably, the maximum specific growth rate constant for NO reduction, μ_{max}^{NO}, is two orders of magnitude higher than for all other N-species. Thus, highlighting the much higher reactivity exhibited by NO, and in agreement with the convention that the kinetics of NO reduction are fast enough to often justify its neglection as an intermediate that merits explicit consideration. However, despite the fast consumption, its accumulation even at nM levels was shown to have pronounced toxic effects in our incubations.

958 **Table S2.** Calibrated parameter values and goodness-of-fit, reported as root mean squared error (RMSE)
959 between simulated and measured values, for both pure-culture incubations of either phototrophs or KS.
960

Phototrophs (SW2)

Parameter	Value	Units	RMSE[1]		
μ_{max}^{photo}	1	[day^{-1}]	*Overall*	0.014	[-]
K_{Fe}^{photo}	32.7	[mM]	*Fe(II)*	0.92	[mM]
Y_{photo}	1.26×10^{13}	[cells mol$_{Fe(II)}^{-1}$]	*Biomass*	2.6×10^{6}	[cells mL^{-1}]

KS-culture

Parameter	Value	Units	RMSE[1]		
μ_{max}^{NO3}	0.43	[day^{-1}]	*Overall*	7.88	[-]
μ_{max}^{NO2}	0.20	[day^{-1}]	*Fe(II)*	1.50	[mM]
μ_{max}^{NO}	77.8	[day^{-1}]	*NO_3^-*	0.13	[mM]
$\mu_{max}^{N_2O}$	0.26	[day^{-1}]	*pNO*	0.04	[Pa]
$K_{NO3/NO2}$	4.0×10^{-3}	[mM]	*pN_2O*	17.9	[Pa]
K_{NO}	3.5×10^{-3}	[mM]	*Biomass*	1.5×10^{6}	[cells mL^{-1}]
K_{N_2O}	3.5×10^{-2}	[mM]			
K_{Fe}^{KS}	7.50	[mM]			
Y_{KS}	3.0×10^{12}	[cells mol$_{Fe(II)}^{-1}$]			
C_{NO}^{thresh}	1.0×10^{-6}	[mM]			
t_d	2	[days]			
p	3	[-]			

[1]RMSE values are reported as overall values, normalized by the measurement standard deviations, or as absolute values per data-type (denoted by italicized text).

961

962

963 **Supplementary Method 2: Parameter uncertainty and sensitivity analysis**

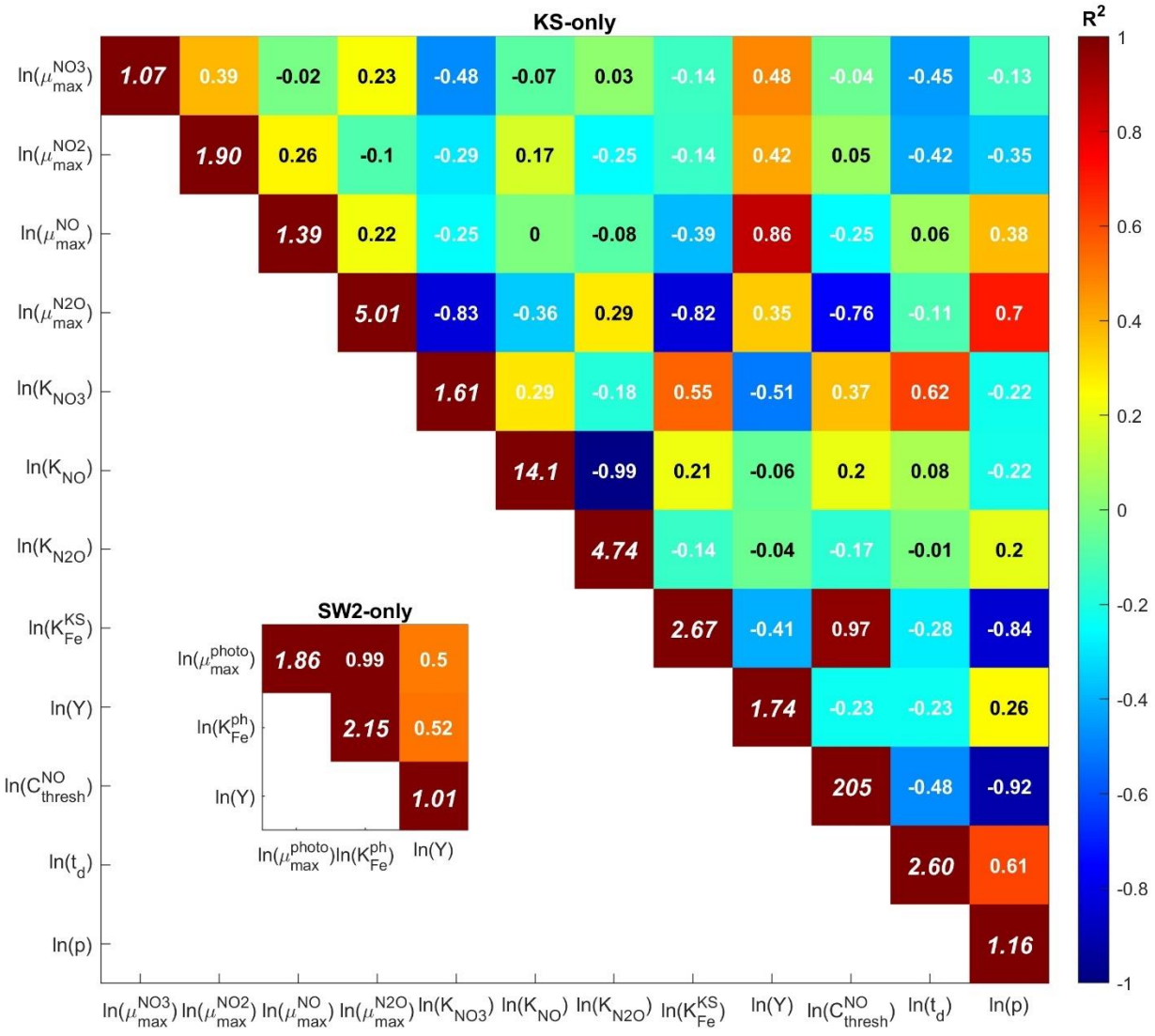

964

965 **Supplementary Figure S11.** Parameter uncertainty correlation matrix for KS- and SW2-only incubations,
966 large and small panels, respectively. The upper triangle (of each panel) shows correlation coefficients of
967 log-parameter uncertainties. The relative errors (×/÷) for each parameter are shown on the diagonal.
968 Parameters with a relative error close to 1 have a low uncertainty.

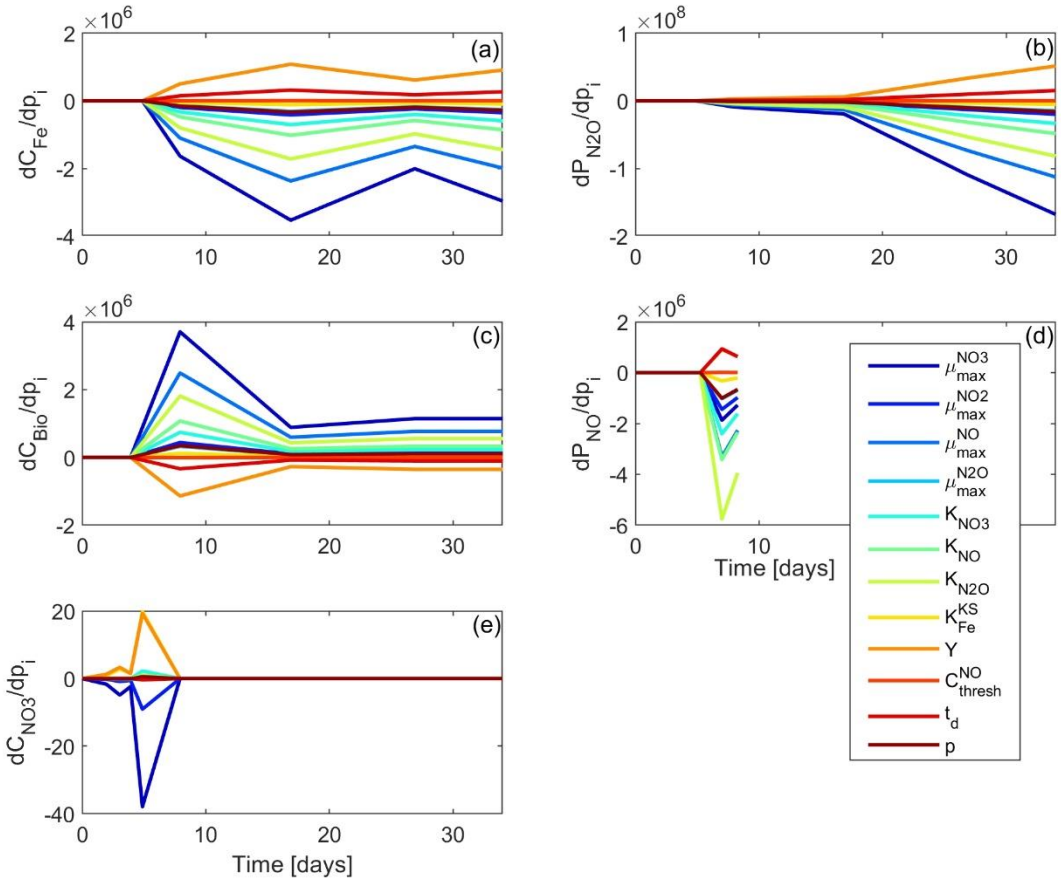

969

970 **Supplementary Figure S12.** Parameter sensitivities plotted at each measurement time point during the
971 KS-only incubation, where i denotes the i-th parameter, listed in order in the figure caption.
972

973

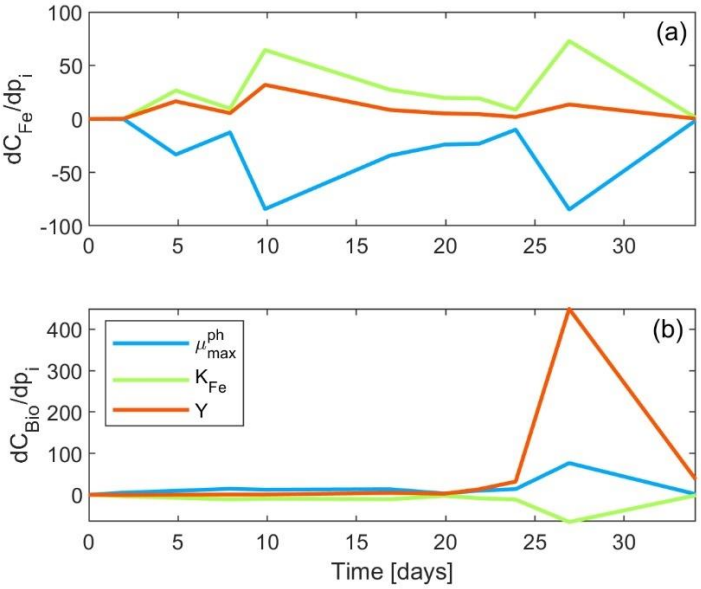

974

975 **Supplementary Figure S13.** Parameter sensitivities plotted at each measurement time point during the
976 SW2-only incubation, where i denotes the i-th parameter, listed in order in the figure caption.
977

Supplementary Data S1. Supplementary information for mapping of nitric oxide detoxification abilities in bacteria, particularly in phototrophs.

***Table 1 Cultured_strains**:* contains information about the presence/absence of genes in the genomes of the four strains of photoferrotrophs that were cultured in this study, as well as the release date of each genome and the BioProject accession number for the corresponding genome sequencing project.

***Table 2 Phototrophs**:* contains information about the presence/absence of genes in the genomes of the 726 phototrophic strains included in the 14618 strains presented in the tree of Fig. 5 and Fig. S9, as well as the accession number for the first sequence in each genome. Phototrophic strains are defined here as possessing at least one of the genes *psaB* (cyanobacterial photosystem I), *pshA* (type I reaction centre), *psbA* (cyanobacterial photosystem II) or *pufL* (type II reaction centre).

***Table 3 Non-phototrophic**:* contains information about the presence/absence of genes in the genomes of the 13892 non-phototrophic strains included in the 14618 strains presented in the tree of Fig. S9, as well as the accession number for the first sequence in each genome.

***Table 4 BLAST_queries**:* contains accession numbers for the sequences that were used as queries in BLAST searches to determine the presence/absence of genes in genomes. Additionally, for each group of genes, i.e., genes for photosynthetic reaction centres (*psaB, pshA/CT2020, psbA1, pufL*); *norV*; *norB* (*cnorB, qnorB*); and *hmp*, a Maximum-Likelihood phylogenetic tree is presented, showing the relationships between the query sequences. As an inset in each tree, the alignment of the corresponding query sequences is shown, highlighting gap regions and including a summary of % identity at each position in the alignment.